Interpretation of Time-Varying Radio Emissions of Sgr A* Observed by 1.3 Millimeter-Wavelength VLBI with Black Hole Binary Concluded by Decameter Radio Wave Pulse Observations

Hiroshi Oya

Geophysical Department, Graduate School for Science, Tohoku University, Space and Astrophysics Research Task, Seisa University, Japan.

*Corresponding author
Hiroshi Oya, Geophysical Department, Graduate School for Science, Tohoku University, Space and Astrophysics Research Task, Seisa University, Japan.

Abstract
In 2011, by 1.3 mm wavelength VLBI radio wave observations of the SgrA, Fish, V. L. et al showed that the emissions tightly related to the formation of a black hole shadow have a remarkably large time-varying feature within a region of less than 50 µas. The present paper suggests that the origin of the time variation in the observed emission is due to effects of the orbital motion of the existing super-massive black hole binary orbiting at SgrA* with a period of 2150±2.5 s. This suggestion is based on observations of decameter radio wave pulses from SgrA*. We show a good correlation between the time variation in the coherent flux density of the VLBI results and the time variation model of estimated emission intensities based on the periodic motion of the super-massive black hole binary by applying parameters deduced from the decameter radio wave pulse observation model (DRWP-Model). With further confirmation by Fourier analyses of the potential periodicity of the VLBI data that show the same periods of DRWP Model, we conclude that the time variation detected by the 1.3 mm wavelength radio wave VLBI is evidence of an existing super-massive black hole at Sgr A*.*

Keywords: Galaxy center, Supermassive Black Hole, Black Hole Binary, VLBI, Millimeter Radio Wave, Decameter Radio Wave, Event Horizon

Introduction

In May 2022, EHTC (Event Horizon Telescope Collaboration) has released the visible shadow image of the event horizon of SgrA*, the supermassive black hole (SMBH) , at the center of the Milky Way Galaxy, corresponding to 1.3 mm VLBI observations [1,-6] after three years delaying from the release of the image of the event horizon of the SMBH, M87* at the center of the elliptical galaxy in the Virgo constellation. [7-12]. The EHTC observations for these two SMBHs were carried out together in April 2017. The delay of release of the SgrA* image is thought as being caused by difficulty to make image for SgrA*; the difficulty involved in capturing an image of the black hole shadow was understood [13] as mainly caused by the time variation that results from the intense scattering of radio waves by electron turbulence in dense plasma. After releases of the images of M87*, however, we meet unexpected stage of the studies on two SMBH images ; though EHTC insists on their results to be no problem[14], there are apparently defects indicating misevaluation to take a hole in collected data as real

black hole in their starting map (image) in their hybrid mapping processes to form the images [15]. Because the data collection system is completely same for M87* and SgrA* cases, we regret to state that the both images are not correct and we should restart for improvement. About the subjects which are directly related to present paper, i,e., time variation of 1.3mm wavelength radio wave intensity surrounding SgrA*, EHTC made wrong selection of ways of data handling [2,3]; EHTC is considering the time variations consist of only random components and try to avoid and to depress to obtain a static image. We, then, show in this paper the essential point of the time variations of SgrA* returning back to the original data before EHTC was organized.

Studies on the time variation in the radio wave flux at SgrA* have grown, starting from the investigation of intermittently occurring flares that were detected by millimeter radio wave telescopes [16-19]. In the history of the research of the time variation in millimeter wavelength radio emissions, epoch making results were provided by Fish et al [20] through 1.3 mm wavelength VLBI observations,

which became the initiation point of the EHT activities [21]; the observation results are characterized by a resolution of a few10 μas , corresponding to the Schwarzschild radius at SgrA*. In studies of the time variation in millimeter wavelength radio wave fluxes, the short time variation in the emissions at Sgr A* has been gradually recognized, not only in times of flare but persisting with a quiescent structure [20,21] and with some periodicity [22].

Independently to the activity of observations by the millimeter wavelength radio-waves from Sgr A*, we continued to investigate Sgr A* to find the spin signature of the event horizon of possible super-massive black holes using decameter radio wave pulses (DRWP) at 21.86 MHz[23]. DRWP observations are not standard for the quest of Sgr A*, because the observation frequency is much lower than the plasma frequencies surrounding SgrA*. Due to the structured magnetic field that is possible in the plasma environment surrounding SgrA*, however, the DRWP can propagate in the form of whistler mode waves that are converted to the ordinary radio waves at points of turbulent and tenuous plasmas as well known in the field of planetary radio-wave science. Furthermore, the source points of decameter radio-waves are possibly located at the region extremely close to the event horizon of the rotating Kerr black hole where the time passage becomes slow due to GR effects. Coinciding with the spin period, therefore, we can observe the decameter radio pulses at the Earth's ground.

Since the start of DRWP observations from SgrA*, it took almost 20 years for convincing results to be reported in 2019 [23]. The principal results revealed two kinds of pulses with intrinsic pulse periods of (173±1) and (148±1) s, showing sinusoidal variation with a common period at 2,200±50 s. By attributing the pulses to spins of two Kerr BHs, we concluded that two SMBHs exist. There are temporarily called Gaa with a mass of $(2.27±0.02)×10^6$ $M_{\odot}$ and Gab with a mass of $(1.94±0.01)×10^6$ $M_{\odot}$ $(4.21±0.03)×10^6$ $M_{\odot}$ in total), and they form a binary system with an orbital period of 2,200±50 s. The orbital velocities of Gaa and Gab are also calculated to be 18% and 22%, respectively, of the velocity of light.

In terms of accepting the results of the DRWP observations, there are arguments that such an extreme super-massive black hole binary system is contradictory because of the possible generation of gravitational waves which exhaust orbiting energy within an extremely short period of time (see Sec. 8.4). However, because it has not yet been experimentally confirmed whether the gravitational waves are generated from the SMBH binary (SMBHB) whose density of matter included within the event horizon is apparently tenuous with a ratio less than 10^{-12} compared to the case of star mass BHs. Then it is worthwhile that the presented SMBHB results are checked using independent experiments such as 1.3 millimeter wavelength VLBI data (VLBI-Data) observations [20,21]. Here, we should emphasize that the recently released image of SgrA* by EHTC that shows a single event horizon is not correct and needed to be reformed.

The motivation of the present study is, therefore, to investigate whether the variation in the intensity and source structure at SgrA* that were detected by the 1.3 mm radio wave VLBI by Fish et al [20,21] are caused by the orbital motion of SMBHB, as concluded by the DRWP observations [23]. It is assumed ,by EHTC, that a variation with short characteristic time (VSCAT hereafter) of several tens of minutes has characteristics of random variation caused through paths of propagating mm wavelength radio-waves due to turbulent plasma media. But we hypothesize that the VSCAT is caused by the orbital motions of SMBHB [23] .Though the approach method of searching for the time variation is different from the intention of Fish et al [20,21] (FEHT hereafter), we consider that the original data published in FEHT are significant when searching for VSCAT information.

For this purpose, we constructed a model of the VSCAT of mm wavelength emissions caused by the orbital motions of SMBHB with orbiting parameters based on the DRWP observations [23] (DRWP-Model hereafter) that give control to the emissions of VLBI-Data that are observed as correlated radio-wave data by VLBI within ~50μas. The principal component of the present work is, then, the comparison of he DRWP-Model with VLBI-Data focusing on VSCAT. The comparison is carried out through fitting processes between the DRWP-Model and VLBI-Data by adjusting the parameters of the DRWP-Model. We express this fitting work as FITW hereafter. The significant principle that is kept currently throughout the FITW is that we never change the parameters resulted from the study on DRWP observations in terms of physics matters of the constructing the DRWP-Model such as the orbiting period range (2200±50 sec), orbiting speeds, and size of the orbits. The adjustment of parameters in the DRWP-Model is only done for numerical components, such as the amplitude related to the flux density, the starting time used to determine the initial timing, and the level in the model to meet with VLBI-Data. In this context, the only exception is the sweeping of the period values. This is not done to find a suitable period from the VLBI-Data but is just for confirmation of how well the DRWP-Model fits the VLBI-Data.

Brief Review of the FEHT and DRWP Observations (Review)
Two selected FEHT works
In the present FITW we mainly refer three works: two by Fish et al [20,21] for VLBI-Data and one by Oya[23] for the DRWP-Model. The VLBI-Data were obtained on three succeeding days from April 5 (95th day) to 7 (97th day) in 2009 by the 1.3 mm wavelength radio wave interferometer with three base lines formed among three stations in the USA: the James Clerk Maxwell Telescope on Mauna Kea in Hawaii (designated J-station), the Arizona Radio Observatory's Submillimeter Telescope in Arizona(S-station), and two telescopes from the combined array for Research in Millimeter-wave Astronomy in California (telescopes C and D). Sources were observed with a high band at 229.601 GHz and a low band at 229.089 GHz, both with a bandwidth of 480 MHz. Using the interferometry correlator at MIT, the system was able to detect the coherency of observed signals for a minimum source size of 10 μas , corresponding to a Schwartzschild radius at 8.3 kpc.

From the two collected papers, here, we focus on VSCAT, mostly by using the correlated fluxes reported in the first paper [20] as VLBI-Data and the VSCAT of the asymmetrical source configuration reported with non-zero closure phase data in the second paper[21] as VLBI-CLP-Data. The time variation data displayed in the bottom panel of Figure 2 [20] is significant from the point of view of investigating the VSCAT for emissions from a compact area within 50μas at Sgr A*. In the first paper of Fish et al, the data are published for S-C (S-D) base line correlation after complete calibration and correction of local deviation of the receiving gains of devices. Corresponding to the displayed data given in Figure 2 of the first paper of FEHT, the original numerical information is given in Table 1 of their paper. From this, we selected the portion of the Sgr A* given for the S-C baseline, as shown in Table 1 of the present work. We refer to Fish et al.'s data through the present FITW as VLBI-Data focusing on VSCAT.

In FEHT published paper [20], it was described that a time variation in the observed data was apparent between observation data collected on the 97th day and those collected on days 95 and 96. The increase in observed power on day 97 was about 17%, which can be attributed to a brightening of the structure on a scale of only a few Schwartzschild radii. Though the authors did not explicitly state this in their paper, there are time-dependent variations in the corrected data that are displayed in Figure 2 of their paper and the corresponding Table 1.

After Fish et al stated the significance of the nonzero closure phase angle to the anisotropy of the source structure in the first paper [20], more extensive reports using the results of EHT group activity were made in a second paper in 2016 [21]. It was concluded that the time variation in the asymmetrical source structure persisted constantly, keeping a quiescent signature. Fish et al [21] stated that it was "likely coupled with some structural variability". Their description is significant to the present paper, because we tried to find the signature of the motion of SMBHB using the VLBI-Data given in Table 1 that were taken from their published data table [20]. We further investigate the coincidence of the time variation with the DRWP-Model with respect to the published results of the closure phase presented in their Table 2 in the second paper [21]. To use their Table 2 only essential parts are taken as given in the present Table 2.

**Table1: VLBI-Data sorted for Sgr A*, from Table1 of Fish et al [20]**

Source	Day Number	UT Time (hh mm)	Baseline	Band	Flux Density (Jy)	σ (Jy)
Sgr A*	95	11 10	SC	Both	2.22	0.13
		11 30	SC	Both	1.86	0.11
		12 00	SC	Both	1.91	0.11
		12 20	SC	Both	1.85	0.1
		12 40	SC	Both	2.06	0.11
		13 25	SC	Both	2.07	0.11
		14 10	SC	Both	2.01	0.11
		15 00	SC	Both	1.79	0.11
	96	11 30	SC	Both	1.98	0.12
		11 50	SC	Both	2.11	0.12
		12 20	SC	Both	2.1	0.13
		12 40	SC	Both	1.95	0.12
		14 15	SC	Both	1.89	0.12
		14 35	SC	Both	1.69	0.12
	97	11 30	SC	Both	2.62	0.17
		11 50	SC	Both	2.68	0.17
		12 20	SC	Both	2.62	0.16
		12 40	SC	Both	2.73	0.18
		13 25	SC	Both	2.91	0.22
		13 40	SC	Both	2.94	0.28

Table 2: Closure Phases taken from Table 2 in Fish et al (2016) [21]

Year	Day of Year	UT Time (hr)	Band	Triangle	Closure Phase (°)
2009	93	11.5417	H	CJS	−21.4
2009	93	11.9583	L	CJS	17.4
2009	93	11.9583	L	DJS	13.3
2009	93	12.2917	L	DJS	−14.01
2009	93	12.6250	L	CJS	−11.1
2009	93	13.1250	H	CJS	9.6
2009	93	13.4583	H	CJS	4.3
2009	93	13.4583	L	CJS	−3
2009	93	13.8750	H	CJS	18.3
2009	93	13.8750	L	CJS	33.7
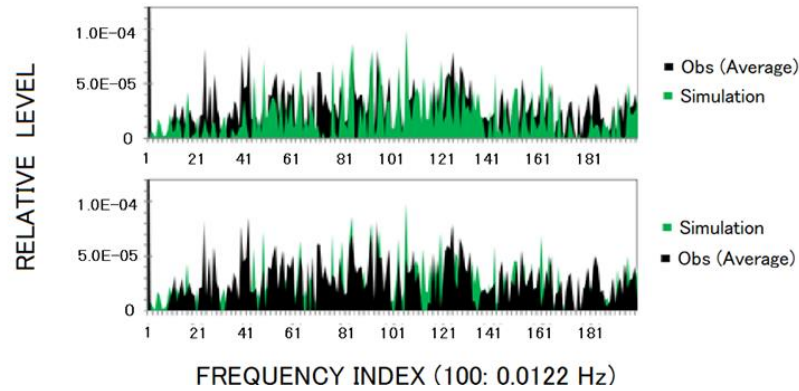
Figure 1: Spectra of the decameter wavelength radio wave pulses from Sgr A* published in 2019 [23]. The relative levels of the analyzed FFT spectra for pulses observed at 21.86 MHz (Black) and the simulation spectra obtained by FFT to express the spinning SMBHB orbiting at 2200±50 s (Green) are indicated overwrapping both in the top panel, where the simulation spectrum is displayed on the front side, and in the bottom panel, where the observation spectrum is displayed on the front side. The abscissa indicates the pulse frequency with a linear index, where index 100 corresponds to 0.0122 Hz. In the given frequency range, a combination of pulses is displayed with higher harmonics up to the third harmonic for both SMBH Gaa and Gab with multiple side bands that are caused by the observed frequency modulation by Doppler shifts due to periodic orbital motion.
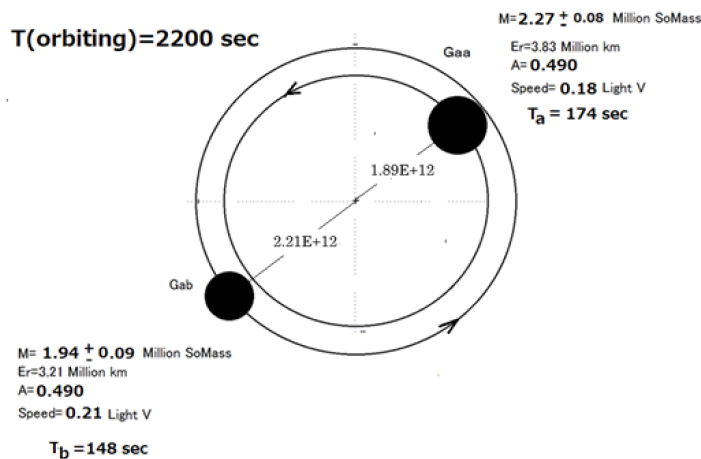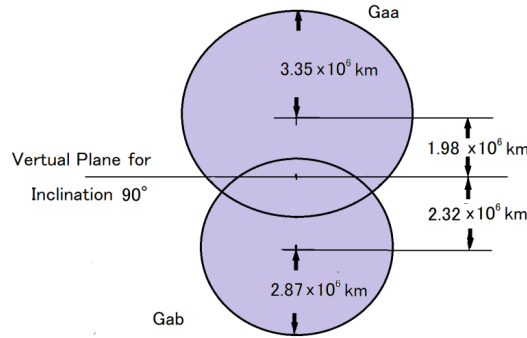

Figure 2: Configuration of the SMBHB concluded by deciphering the analyzed FFT spectra for the decameter wavelength radio waves from Sgr A*, assuming that the pulse frequencies are synchronized with spins of SMBHs Gaa and Gab that are subjected to the Doppler effect due to orbital motion. The distance between two SMBH is 2.84 R_{ss} with respect to the Schwartzschild radius R_{ss} if we assume that there is a single black hole (Radii of two BH are given by the unit cm) .

DRWP Observations [23]

At Tohoku University, by using a long baseline interferometer for decameter wavelength radio waves consisting of three antenna sites with baseline lengths ranging from 44 to 83 km at 21.86 MHz, we observed decameter radio wave pulses from Sgr A* at our Galaxy center, mainly in June 2016 and June 2017. Because of the extremely low S/N (signal to noise ratio), where the background noise levels were 300 to 500 times larger than the signal levels, the observed interferometer data were analyzed uniquely to detect the source direction using the Earth's rotation. Separation of the signal from the high background noise was accomplished by applying the Interferometer Fringe Function Correlation Method (IFFCM, see

[23]), where the aperture synthesis method of the interferometer data that utilize the Earth's rotation, was modified to eliminate any ambiguity of local phase shifts in the system as well as phase shifts due to ionosphere propagation. Pulse forms in the signal were confirmed in the Fourier-transformed domain by applying FFT operations to the time series data of the IFFCM. By taking an average of the FFT results over 2016 independent sets, the pulse frequencies were discriminated from the background white noise. The resulting signals indicate the source direction at Sgr A* within ±6 arc minutes. Further, the final data, called the BH code, (see Figure 1) were deciphered by applying the simulation; that is,

Figure 3: Geometrical configuration of the view from the observation points at the time of the maximal eclipse phase of two SMBH, Gaa and Gab. The orbital plane surface of the SMBHB is tilted by 6° from the direction parallel to the line of sight from the observation point.

the function of time variation for the FFT analyses has been constructed to represent the SMBHB system where two spinning Kerr BHs are radiating decameter radio waves whose intensities are synchronized with spins that are subjected to orbital motions indicating spin frequency variations due to Doppler effects caused by the orbital motions. The matching of FFT spectra between the observation results and the simulation results shows the existence of two kinds of pulses; that is, the detected intrinsic pulse periods of (173 ± 1) and (148 ± 1) s show sinusoidal variation in the period values with common periods at $2,200\pm50$ s. By attributing the pulses to spins of two Kerr BHs with the maximum rotation parameter, the masses of the two BHs were deduced with additional Newtonian dynamics information obtained from orbiting parameters such as the orbit radii, the orbiting period, and the orbiting velocities deduced from the Doppler effects. We have concluded that two supermassive BHs exist, temporarily called Gaa with a mass of $(2.27\pm0.02)\times10^6$ $M_\odot$ and Gab with a mass of $(1.94\pm0.01)\times10^6$ $M_\odot$ $((4.21\pm0.03)\times10^6$ $M_\odot$ in total), forming a binary system with an orbital period of $2,200\pm50$ s, as given in Introduction. In Figure 2, the configuration of the SMBHB at Sgr A* is depicted with parameters selected from Tables 9 and 10 of the paper [23]. To deduce the black hole masses, we assumed that we were observing the orbital motion from the direction parallel to the surface of the orbital plane. ; as it is described in the next Sec. we are required a slight correction for the looking angle of the orbital motions.

Construction of the DRWP-Model to show the Origin of Time Variation for the VLBI-Data
Eclipse effects due to the orbital motion of the SMBHB
In the present study, we hypothesize that the origin of the VSCAT in the VLBI-Data is mainly related to the motion of the SMBHB, except for the time of flare [16-19] ; in the case of gradual variation of background condition [20], the model is still applicable. Two

effects are considered to generate VSCAT emissions at SgrA*, and these were detected within the 50 μac range by the 1.3 mm wavelength VLBI. These are the eclipse of the orbiting SMBHB and spectral shift due to Doppler effects caused by the fast speeds of the SMBHB orbital motion.

Here, we first describe the eclipse effects. To conclude that the total mass of the SMBHB is $M_D=(4.21\pm0.03)\times10^6$ $M_\odot$, we assumed that the inclination of the orbital plane surface is parallel in the direction of the observation line of sight, with θ_I being close to 90.° Regarding the accuracy of the θ_I value, however, there is a room for correction when we refer to the BH mass obtained from the effects of gravity on the motion of surrounding stars, which was determined to be $M_{CD}=(4.28\pm0.31)\times10^6$ $M_\odot$ by Gillessen et al. [24]. (GSM, hereafter). By attributing the difference in the masses deduced from DRWP observations and GSM to the assumption of the inclination of the orbits of the SMBHB, we have deduced correction angle $\Delta\theta$ to θ_I (= 90°) . As details are given in Appendix-A, the relationship of the total mass M_D of the SMBHB to M_{CD} of GSM is

$$M_{CD} = \frac{M_D}{sin^3\theta_I^*} = \frac{M_D}{cos^3\Delta\theta} . \qquad (1)$$

where $\theta_I^*=\pi/2-\Delta\theta$,with units of radians. Then, the angle $\Delta\theta$ can be expressed as

$$\Delta\theta = \sqrt{\frac{2}{3}\cdot\left(\frac{M_{CD}}{M_D}-1\right)} . \qquad (2)$$

By taking the central values of the given M_{CD} and M_D as the most likely values, we have determined the $\Delta\theta$ value to be 0.105 radians (6.0 degrees). As shown in Figure 3, the orbiting radii of Gaa and Gab are 1.89×10^7 km and 2.21×10^7 km, respectively.
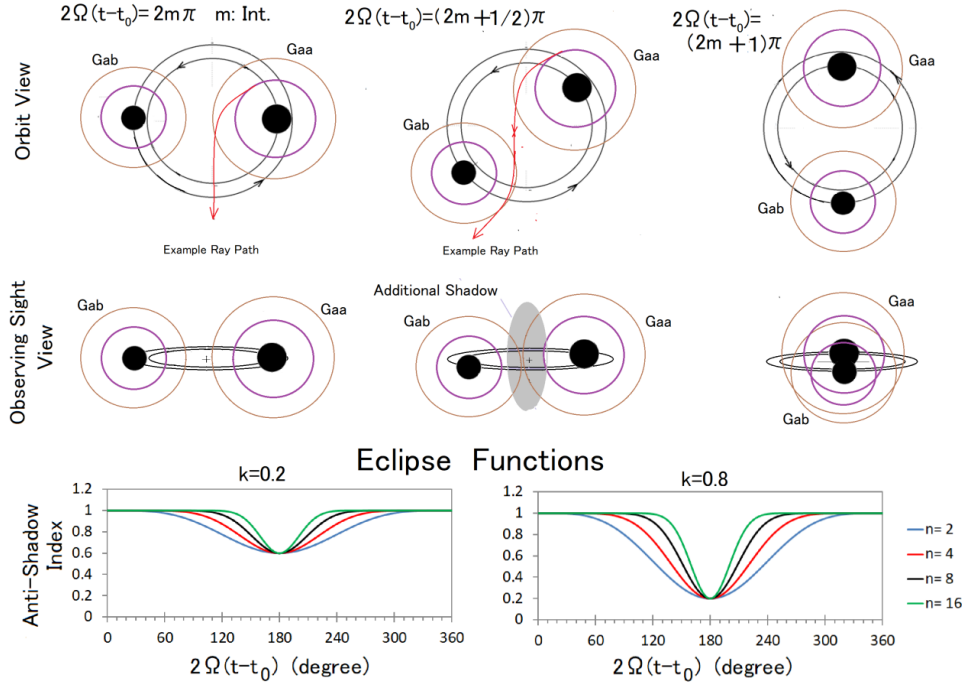
Figure 4: Model of the SMBHB eclipse between Gaa and Gab. Three eclipse phases are illustrated as the orbital view looking down from the vertical direction of the orbital plane in the top line for three phases at different moments in time, $2\Omega(t-t_0)= 2m\pi(\text{Rad})$, $2\Omega(t-t_0)=(2m+1/2)\pi$ (Rad) and $2\Omega(t-t_0)=(2m+1)\pi$ (Rad), for the integer m with an arbitrary starting time t_0. Corresponding to each phase observation, sight views are depicted in the middle line. In all views and phases, SMBHs are depicted as being associated with two rings; the first ring has radius of $3r_g$ (r_g is the gravitational radius that is given by $r_g=GM/c^2$ for a constant gravity G, mass M, and light velocity c), which is given as a reference to estimate the curvature of the light path. The second large circle has a radius of $5r_g$, which shows the approximate shadow limit for emissions from sources surrounding the rotating black hole. The red curves in the first and second phases in the line of the orbital view are examples of ray paths to show the qualitatively estimated gravity effects on the propagation of radio waves. In the bottom line, two cases of eclipse function are shown for coefficients k=0.2 and k=0.8 with the corresponding parameter n. These are indicated to model the emissions feature versus the eclipse phases $2\Omega(t-t_0)$.

A shift in the inclination by 6.0° results an upward shift of 1.98×10^6 km from the virtual orbital plane assumed for a pure vertical inclination with respect to the line of the sight for the center of Gaa, whose radius of the event horizon is 3.35×10^6 km. A downward shift of 2.32×10^6 km, also from the virtual plane, is deduced for the center of Gab, whose radius of the event horizon is 2.87×10^6 km (see Figure 3). The upper and lower positions of both partner BHs in the SMBHB system, with respect to the virtual plane, are switched alternatively at each coming maximal phase of the eclipse. Then, we observe twice of the decrease of emission power in every orbiting period of 2200 ± 50 s. Based on the 6.0° tilt of the SMBHB orbit plane surface from the pure parallel direction with respect to the line of sight, we construct a function of the DRWP-Model for comparison with the VLBI-Data. Deferring highly accurate quantitative analyses of the eclipse effects for future work, here, we only consider a qualitative ray paths effects subjected to the intense gravity condition in the spacetime of Kerr black holes that form the SMBHB. In Figure 4, we depict the configurations of the Gaa and Gab SMBHB for three sampled phases of mutual motion along the orbits of the SMBHB, together with functions to express the eclipse effects (Bottom two

diagrams). The two SMBHs on the binary orbits, Gaa and Gab, are depicted using the orbit view looking down the orbital plane and using the view from the observation sight for three phases of the positions of the SMBHB. In the figure, we express the orbital motion of the SMBHs with the angular velocity Ω. Then, in Figure 4, the positions of the SMBHs Gaa and Gab at the first, second, and third phases correspond to the moments when $2\Omega(t-t_0)= 2m\pi(\text{Rad})$,$2\Omega(t-t_0)=(2m+1/2)\pi$ (Rad) and $2\Omega(t-t_0)=(2m+1)\pi$ (Rad) with integer m and time t, measured from an arbitrarily selected start time t_0. In all the views and phases shown in Figure 4, the SMBHs are depicted as being associated with two rings; the first ring has a radius of $3r_g$ (r_g is the gravitational radius given by $r_g=GM/c^2$ for the gravity constant G, mass M, and light velocity c), which is given as a reference to allow better understanding of the curvature of the light path. The second large circle has a radius of $5r_g$ which shows the approximate shadow limit. We refer to the case of the non gravito magnetic effect shown by Abdujabbarov,et al. [25] for emissions from sources surrounding a rotating black hole.

We have constructed a model function to reflect qualitatively describe the state of the eclipse of radio emissions surrounding the

SMBHs phase-by-phase, as given in Figure 4.
- The phase at 2mπ: This is the phase where two SMBHs, Gaa and Gab, are separated with the maximum separation phase angle seen in the observation areas. We observed maximum emission power from the two SMBHs. In this phase, shadows at each SMBH exist inherently without depending on the mutual separation angle. We describe the emission power in the 1.3 mm wavelength range as the total situation in the region of bright emissions together with the individual shadow and lensing ring regions, as seen in the M87* image [7-12]. (The exact feature should be different though). In this phase, we can also recognize that the propagation of the radio waves towards the observation areas may not be hindered by the effects of gravity from the partner BH, as depicted by the example ray path (red curve) that starts from the region at about $3r_g$ from the center of the SMBH Gaa. To approximately depict the ray path under intense gravity conditions, we consider the situation qualitatively with reference to the curving ray path using a rough estimation method of simplified general relativity, because we are not required to have accurate solution as is the case solving null geodetics [eg,26], which is the most essential approach for ray tracing. The rationale for using the method of simplified general relativity is explained in Appendix B.
- The phase at (2m+1⁄2)π: This is an example case of the intermediate position of two SMBHs before approaching the maximal phase of the eclipse. As depicted by an example ray path (red curve), the ray path that is hindered by the gravity effect of the partner SMBH starts to appear. The radio emissions are decreased gradually as the motions of SMBHs approach the maximal phase of the eclipse.
- The phase at (2m+1)π : This is the maximal phase of the eclipse; the two SMBHs overwrap with a slight vertical shift with respect to the orbital plane, as explained in Figure 3. The shadow effects are not limited to shading by the disk of the front SMBH with the radius of the event horizon, but the effect of shadow formation by the partner SMBH moving behind is expanded to the range of the SMBH's own gravity lens. Then, the total emissions from the two SMBH environments are depressed to the minimum level for the entire phase of the mutual positioning of the two SMBHs.

In the bottom two panels in Figure 4, the constructed eclipse functions are indicated with the functional form $E_c(t)$. We selected a simplified function to express $E_c(t)$, assuming that the same effects occur for two SMBHs in the cases of shading of the partner SMBH. Therefore, the same rate of eclipse shading takes place twice alternatively within a revolution of orbital motion; that is,

$$E_c(t) = 1 - k \left[\frac{1 - cos2\Omega(t - t_0)}{2} \right]^n.$$ (3)

where n is an index to control the effective interval of the eclipse,

and k is the rate of emission shaded by the partner SMBH at the maximal phase of the eclipse. On the left and right sides of the bottom line diagrams shown in Figure 4 , the cases of k=0.2 and k=0.8 are displayed with parameters of n=2, 4, 8, and16. In the FITW processes between the VLBI- Data and the DRWP-Model, these n values are varied to find the best fitting case.

Variation in the observed spectral shift due to Doppler effects

Though the effects of the time variation in the observed VLBI-Data are weak compared with the eclipse effect of the SMBHB, the possibility of time variation when observing VLBI-Data can be considered. Except for the case of burst time radiation, the power law spectra of the radio emissions from Sgr A* is known to have the index of 0.3 [27]. In the regular state of the average condition of the accretion of the plasma, we assume that the radio wave emission spectra $P_j(\omega)$ for SMBH- j (j=Gaa or Gab) is

$$P_j(\omega) = K_j f^{0.3}.$$ (4)

where f is the emission frequency at the sources, and K_j is a constant coefficient that reflects all electromagnetic environments related to the radio wave emissions from each member j of the SMBHB. The observed frequency f_{ob} is related to the source frequency f that is subjected to the Doppler effects of orbiting SMBH-j as

$$f_{ob} = f \cdot \left[1 - \frac{v_j}{c} sin\theta_I cos\Omega(t - t_0) \right]$$ (5)

where v_j and t_0 are the orbiting velocity and arbitrary time when SMBH Gaa is at the zero Doppler effect position for SMBH-j ; θ_I is an angle between the sight direction from the observation point and the normal direction of the orbital plane (Determined to be 84.0° ,see Sub Sec 2.1) . Then, the source frequency f that provides the observation frequency f_{ob} is given by

$$f = \frac{f_{ob}}{1 - \frac{v_j}{c} sin\theta_I cos\Omega(t - t_0)}.$$ (6)

We selected v_{Gaa}/c=0.18 and v_{Gab}/c=0.21 in accordance with the DRWP results [23]. Thus, eq.(6) can be approximated as

$$f = f_{ob} \left[1 + \frac{v_j}{c} sin\theta_I cos\Omega(t - t_0) \right].$$ (7)

Considering eq.(4), therefore, the emission power $P_{dj}(f_{ob})$ detected by observation points at f_{ob} for each SMBH-j is expressed by

$$P_{dj}(f_{ob}) = K_j \left\{ f_{ob} \left[1 + \frac{v_j}{c} sin\theta_I cos\Omega(t - t_0) \right] \right\}^{0.3}.$$ (8)

Considering the values v_j/c, again, $P_{dj}(f_{ob})$ is given by

$$P_{dj}(f_{ob}) = K_j f_{ob}^{0.3} \left[1 + \frac{0.3v_j}{c} sin\theta_I cos\Omega(t - t_0) \right].$$ (9)

To obtain the total emission power from the SMBHB, we apply the eclipse effects together with the simple addition of two individual spectra variations.

Total model function to express the time variation due to SMBHB orbital motion

The emissions of partner SMBH-j that are shaded by the eclipse switch alternatively between Gaa and Gab. In the equation, to express the time-varying power, we defined a switching function $S_j(t)$; thus, the model of the time-dependent emission power $W_T(t)$ from the SMBHB at Sgr A* is

$$W_T(t) = \left\{ K_{Gaa}f_{ob}^{0.3}\left[1 + \frac{0.3v_{Gaa}}{c}sin\theta_I cos\Omega(t-t_0)\right]S_{Gaa}(t)\right.$$
$$\left. + K_{Gab}f_{ob}^{0.3}\left[1 - \frac{0.3v_{Gab}}{c}sin\theta_I cos\Omega(t-t_0)\right]S_{Gab}(t)\right\}E_c(t) \qquad (10)$$

where $S_{Gaa}(t)$ and $S_{Gab}(t)$ are defined as follows

$$S_{Gaa}(t) = \begin{cases} 1 & for \ \ 2m\pi \le \Omega(t-t_0) < (2m+1)\pi \\ 1/E_c(t) & (2m+1)\,\pi \le \Omega(t-t_0) < (2m+2)\pi \end{cases}$$

and

$$S_{Gab}(t) = \begin{cases} 1/E_c(t) & for \ \ 2m\pi \le \Omega(t-t_0) < (2m+1)\pi \\ 1 & for \ (2m+1)\pi \le \Omega(t-t_0) < (2m+2)\pi \end{cases} \qquad (11)$$

Selection of parameters to Construct the DRWP-Model
Power ratio between Gaa and Gab

The ratio of the radio wave emission power of Gaa and Gab at the 1.3 mm wavelength is strictly related to the environment, where the source energy is fed by accreting plasma from the outside and the efficiency with which the energy of accreting plasma is converted into radio wave emissions. In this context, we can conclude that there is no apparent difference for the accreting plasma condition between the two SMBHs because of their similar orbit situations in the SMBHB. Regarding the conversion efficiency, the slight differences in the masses and sizes of the two SMBH may affect the processes by which the radio waves are generated. From a macroscopic estimation point of view, black holes have, however, constancy in their radio wave emissions energy. It is well known that the intensity of radiated electric and magnetic fields of radio waves is proportional to the acceleration of the charged particles at the sources. When we describe the macroscopic features of the radio-wave emission energy from the Schwarzschild BH, for simplicity, the total power W_T can be expressed as

$$W_T = K\left[\frac{GM}{(\eta r_g)^2}\right]^2 4\pi(\eta r_g)^2 = 4\pi K\left(\frac{GM}{\eta r_g}\right)^2. \qquad (12)$$

where η is a coefficient to indicate the region of interest in units of the radius of gravity, and K is the coefficient of energy conversion in units of area. Because $GM/r_g = c^2$, it follows that

$$W_T = 4\pi K\frac{c^4}{\eta^2}. \qquad (13)$$

Because of the plasma environment and region of interest for the emissions of mm wave length wave radiation from a macroscopic point of view, we can take K and η as being almost the same for Gaa and Gab SMBHs; thus, we set the ratio of the radio wave emissions between Gaa and Gab to be unity.

Using this assumption and the already presented v_{Gaa}/c and v_{Gab}/c values, together with $\theta_I = 90° - 6.0°$, we can express eq.(10) in a simplified form as

$$\overline{W_T(t)} = \{[1 + 0.0537cos\Omega(t-t_0)]S_{Gaa}(t)$$
$$+ [1 - 0.0626cos\Omega(t-t_0)]S_{Gab}(t)\}E_c(t) \qquad (14)$$

where $\overline{W_T(t)} \equiv W_T(t)/(K_{Gaa}f_{ob}^{0.3})$. At this point, we recognize that the effects of time variation when observing emission spectra are minor with a rate of about 20% compared with the effects of the eclipse on the time variation, which indicates the rate k (=0.3) for shading the observing emissions from one of the SMBHs.

Setting the parameters
Amplitude and Bias

Using this model function as the DRWP-Model based on data from the DRWP observations, we carried out a FITW (comparison with VLBI-Data). For this purpose, we are required an additional adjustment by introducing the amplitude A(m) to match with the observation level given by the VLBI-Data, because the function of the DRWP-Model given by eq.(14) is expressed only as relative quantity that is normalized by the 1.3 mm wavelength emission power of the SMBH Gaa. The amplitude A(m) is given as a function of the observation day m where m=1,2 and 3 correspond to days 95, 96 and 97 in 2009, respectively, when the observations of VLBI-Data were carried out. Furthermore, we introduce another parameter, Bias(m), to represent the emission power in the 1.3 mm frequency range from the accreting plasma environment surrounding the SMBHB that is not directly related to the movement of the SMBHs. Thus, we have prepared the

final form of the model function Mod (t,m) as the DRWP-Model starting from eq.(14) as

$$Mod(t, m) = A(m)\{[1 + 0.0537 \cdot cos\Omega(t - t_0)]S_{Gaa}(t) \quad (15)$$
$$+ [1 - 0.0626 \cdot cos\Omega(t - t_0)]S_{Gab}(t)\}E_c(t) + Bias(m)$$

For decision of the parameters A(m), and Bias(m), we tried to find the best fitting values by sweeping the possible range for each parameter.

Period and Initial Phase angle

The most important parameter for the FITW is the period of the VSCAT in the VLBI-Data. Because of the principal purpose of the present study, we set the period range according to the results of the DRWP observations, which indicated the period of T=2200±50 s. Then, we search T to find the best fit by sweeping T in a range from (2200-70) *s to* (2200+70) s with expanding the range by ±20 s.

The second significant parameter for the FITW is the initial phase, which is controlled by the time t_0 in eq. (15). Taking t=0 as 11:00 h UT time on the 95th day of VLBI-Data observations, we tried to sweep the whole range from 0 to 2π Rad as the initial phase angle Ωt_0 with a step of $(5\pi/360)$ Rad. This selected initial phase is kept throughout the entire 3 day data collection period until the end of the VLBI-Data observations. It should be emphasized that fitting in the FITW is conducted with strict constraint to keep the phase consistent throughout the entire 3day period for the DRWP-Model to avoid making an arbitrary phase shift for adjustment at each local time spot.
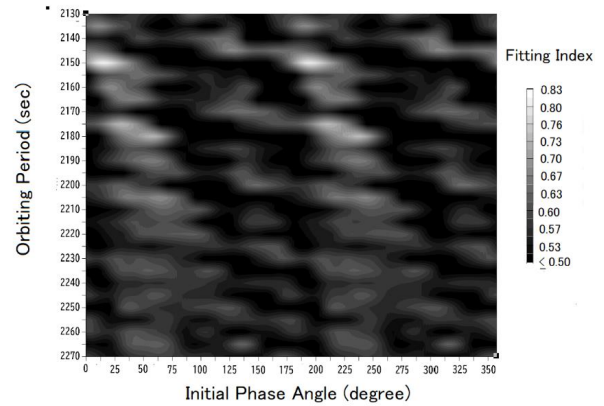
Evaluation Index

To decide the best fitting point objectively, we defined the evaluation index based on Gaussian statistics for the values to show coincidence between the VLBI-Data and DRWP-Model. Considering the standard deviation value σ_i associated with data points VD(t_i) at the observation time t_i (Fish et al, see Table 1[20]), we set the argument of coincidence ξ_i as

$$\xi_i = (VD(t_i) - DM(t_i))/\sigma_i. \quad (16)$$

where DM(t_i) is the DRWP-Model value at the same time t_i. Because there are many factors that bother the coincidence between two values, it is reasonable to consider the Gaussian stochastics to evaluate the significance of ξ_i. To set the index to be unity when all 20 data points coincide with the model values, and considering the situation where the occurrence of coincidence is independent between each data point at t=t_i, we define the evaluation index I_c as follows:

$$I_c = \frac{1}{20}\sum_{i=1}^{20} exp\left[-\frac{\xi_i^2}{2}\right]. \quad (17)$$

Figure 5: Gray code display of the evaluation indices I_c for the fitting results between the VLBI-Data and DRWP-Model versus the orbiting period of the DRWP-Model (with n=4) and the initial phase angle (°) at 11:00 h UT on April 5, 2009. The results are given for period (range of 2130 to 2270 s) versus the initial phase angle (0 to 360 degrees) set at 11:00 UT on the 95th day. We can see that there are 6 candidates for period and initial phase combinations: two cases with a period of 2150 s, two cases with a period of 2175 s, and two cases with a period of 2180 s.

With this evaluation index, we have tested whether the VLBI-Data are time-varying or not using a constant as the average value. For this subject, the calculated index is 0.54. The meaning of this index value is that there is a 50% possibility of the VLBI-Data points being constant vs. varying. We can state, then, that the VSCAT may be either constant or varying, depending on the standing

Table 3: Determined Parameters: Amp (m), Bias (m), and k.

Applying Day (m)	Amplitude Amp(m)	Bias Bias(m)	Coefficient k
95 (m=1)	1.37	−0.61	0.24
96 (m=2)	1.41	−0.76	0.24
97 (m=3)	1.44	0.06	0.24

points approaching the subject of concern. Because our approach to VLBI-Data was to clarify the state of VSCAT, we are required to find an index that appears to be higher than 0.54. The evaluation of the fitting index amplitude parameter A(m), bias parameter Bias(m), and the coefficient k to construct the eclipse function are given in Table 3.

Fitting Results
Confirmation of the period of VSCAT(variation with short characteristics time)

In Figure 5, the fitting index I_c of the FITW results given for n=4 for a period range of 2130 to 2270 s versus an initial phase angle of 0 to 360 degrees show 6 candidates and initial phase combinations; two cases with a period of 2150 s , two cases with a period of 2175 s, and two cases with a period of 2180 s. The evaluation indices of these candidates are given in Table 4. Apparently, these 6 candidate

cases consist of 3 pairs of results whose initial phase angles can be related by shifting π Rad for the second peaks of the fitting index at the same period. By investigating the total 6 candidate cases, we concluded, using the results of the FITW, that a period of 2150 s with an initial phase angle of 15° is the best fitting case with the maximal I_c index of 0.811.

Figures 6 to 8 show the FITW results for the three cases of the eclipse model with n=2, 4, and 8. It is clarified that the DRWP-Model fits the VLBI-Data well, suggesting the significance of the VSCAT with a systematic period of around 2150 sec.

In Table 5 the fitting indexes are shown as the FITW results for three eclipse models.

Table 4: Local Maxima of the Fitting Index

Period (sec)	Initial Phase (°)	Fitting Index
2150	15	0.811
2150	195	0.803
2175	30	0.737
2175	210	0.740
2180	57.5	0.737
2180	237.5	0.744

Table 5: Fitting Index for Three Eclipse Model

| Eclipse Model n	Period (sec)	Initial Phase (°)	Fitting Index
2	2150	17.5	0.791
4	2150	15	0.811
8	2150	15	0.792
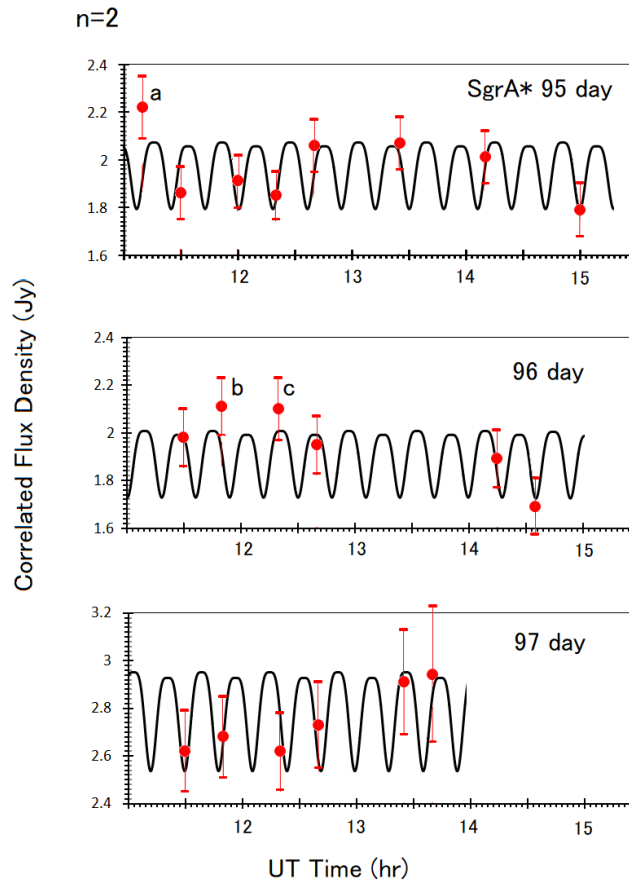
Figure 6: The results of the FITW for three observation days, from April 5 (95th day) to April 7 (97th day) in 2009 with the DRWP-Model with an eclipse function of n=2. The red spots with error bars are the VLBI-Data series presented by Fish et al [20] and the black curves are the DRWP-Model.

with n=2, 4, and 8. Though there are slight differences among the three models, the results show that all cases have sufficiently high Ic values, giving us 80% confidence to conclude that the FITW is successful. In terms of concluding that fitting was complete, however, three data points given by the labels a, b, and c in the diagrams in Figures 6, 7, and 8, show deviations around σ. Considering these data do still not depart from the error bar limit and owe only 15% in relation to all other data, we consider that these three data points do not negate the conclusion of a successful FITW.

Significance of the Period Selection

As has been stated previously, the most significant parameter in the present FITW is the period T when searching for the VSCAT in the VLBI-Data. To make a firm conclusion, we expanded the period range from the initial setting based on the DRWP observation result of 2200 ± 50 s to a wider range of 1550 to 2850 s. In Figure 9, the
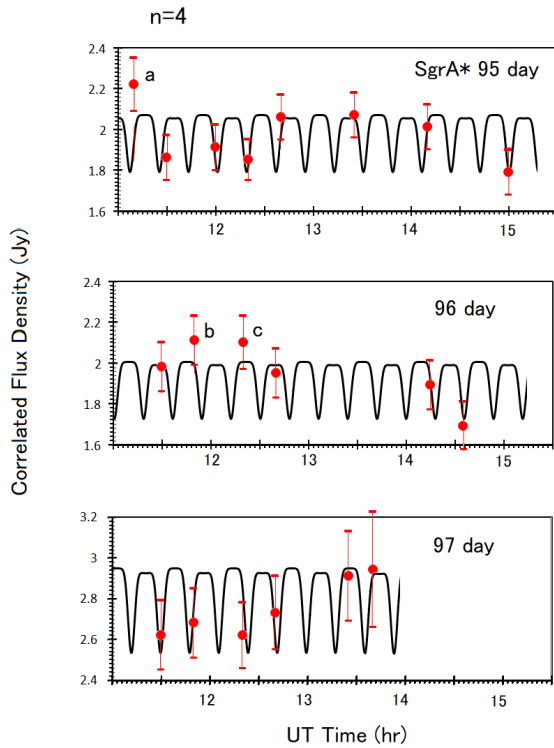
Figure 7: As with Figure 6 but for the case of the eclipse function parameter n=4 in the DRWP-Model.
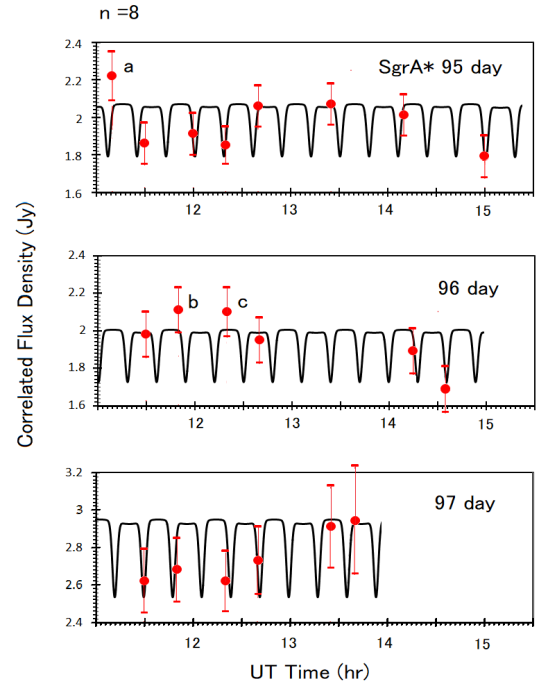
Figure 8: As with Figure 6 but for the case of the eclipse function parameter n=8 in the DRWP-Model.
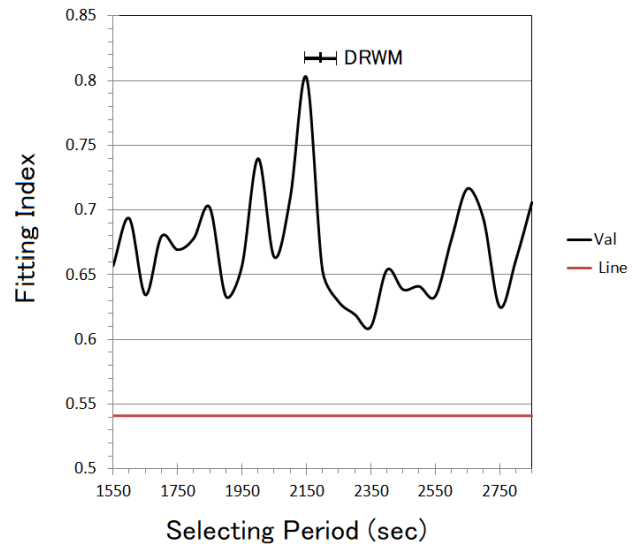
Figure 9: The fitting index Ic for the maximal case for each period in the range from 1550 to 2850 s. DRWM indicates the period range of 2200 ± 50 sec that was determined by the decameter radio wave pulse observations [23] . The red line shows the fitting index Ic for hypothetical assumption of constant VLBI-Data.

the fitting index Ic for the maximum case at each period in the range from 1550 to 2850 s is indicated together with Ic =0.56 (Red line) as a reference to show the assumption of constant VLBI-Data. It is remarkable that there is a single maximum within the

period range at the period of 2150 s, which coincides with the DRWP prediction, although the peak occurs right at the minimum limit of the DRWP prediction (see Figure 9).

Before stating that the VSCAT is a complete manifestation of the SMBHB effects, we need to carefully check the present FITW processes, because we are analyzing the time variation within the restrictions of the data sampling time window. We will investigate this using other approaches. One is involved in additional work on the closure phase data provided by Fish et al [21]. The second is the approach by the Fourier transformation that reveals the potential periodicity of the time-varying component of the data.

VSCAT in the closure phase data
Model of the rotating asymmetry fitted to the VLBI-closure phase

The closure phase related to VLBI-Data contains significant information on the structure of the source region within 50 μas, as pointed out by Fish et al [21] as has been described in the Introduction and Review sections in the present paper.

We have tried to find the VSCAT by applying the periodicity of orbital motion of SMBHB with respect to the closure phase data provided by FEHT (see Sec. Review) that are reproduced for the VSCAT related portions (VLBI-CLP-Data). As pointed out in the original paper by Fish et al, [21], the closure phase data are a manifestation of the
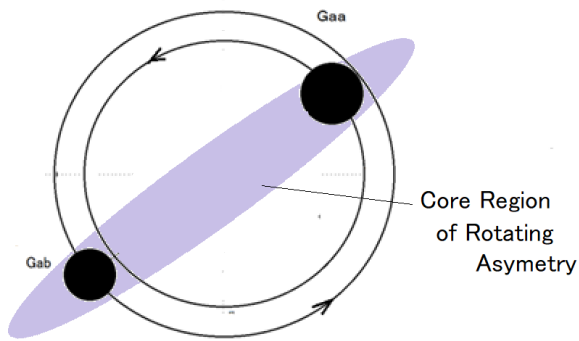
Figure 10: Assumption of a rotating bar structure that represents the SMBHB orbital motion observed at remote points. The distance between Gaa and Gab corresponds to 40 μas, as shown by the results of DRWP observations. It seems to rotate twice within a SMBHB orbiting period of 2200±50 s.

asymmetrical structure of the radiation sources. Based on the DRWP results [23] , we have assumed that there could be the existing VSCAT in the VLBI-CLP-Data whose time variation could be synchronized with the orbiting motion of the SMBHB. In Figure 10, a model of rotating asymmetry is shown on the basis of the SMBHB results presented in the DRWP study. Because the asymmetry is caused by aligning two SMBHs, Gaa and Gab, the asymmetrical region formed with a bar-like structure rotates

with an orbiting period of 2200 ± 50 s . The line of sight of the interferometer observation stations is almost in a parallel direction to the orbital plane. The bar structure occupies a similar position two times within one rotation of the orbital motion of the SMBHs. We constructed a simplified model (DRWP-CLP-Model) to make the possible occurrence of the closure phase θ_{CL} detectable by the interferometer with triangle baselines as

$$\theta_{CL} = \theta_{Max} cos[2\Omega(t + t_0)] . \qquad (18)$$

where $\Omega = (2\pi/T_{orb})$ with the orbiting period of the SMBHB T_{orb}, and θ_{Max} is the possible maximum closure phase angle.

In Figure 11, examples of FITW with the VLBI-CLP-Data are given for two cases of the DRWP-CLP-Model with setting periods of 2105 and 2200 s with the fitting index Ic for each. The definition of the fitting index is the same as that given in eq.(17), but the amount of data for this case of the closure phase is limited only by 10 points where two data points coming from the Low and high frequency channels are overwrapped, forming a pair at the same sampled time for the three cases given in Table 2. We used all data as principle but avoided the last data point observed on the 93rd day 13.8750 h, because it appeared to deviate from the trend of the other data. observed on day 93 in 2009 .
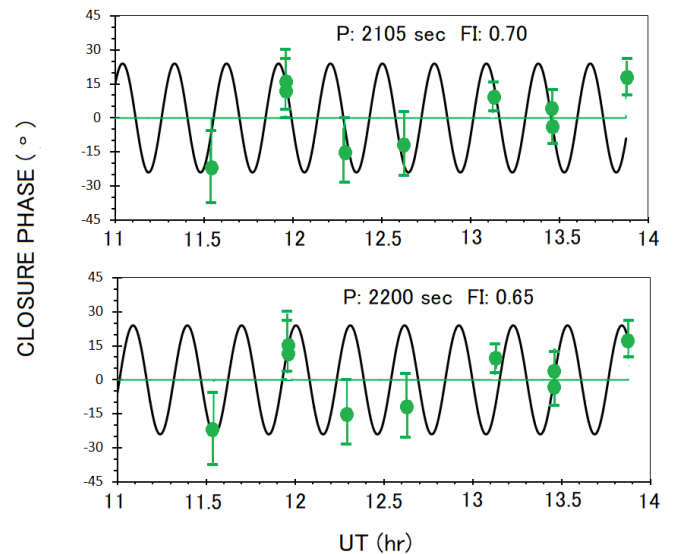

Figure 11: Fitting of the DRWP- CLP-Model (black curves) with the, VLBI-CLP-Data (green spots) observed on day 93 in 2009 . Two orbital periods are set for DRWP-CLP-Model as 2105 s (top panel) and 2200 s (bottom panel). The fitting index (FI) is indicated in the each panel.

Two orbital periods are set for DRWP-CLP-Model as 2105 s (top panel) and 2200 s (bottom panel). The fitting index (FI) is indicated in the each panel. The σ values are not indicated in Table 2 of the second paper [21] for FEHT, but in Figure 2 of their paper, σ values for the corresponding data are recorded, and these are usable for the present analysis of the fitting index.

In this FITW, the assumption of there being no VSCAT for this time series of the closure phase data gives a fitting index of 0.564. We understand that no VSCAT condition has a likelihood of about 50%. In a paper on persisting time variation reported by FEHT, only a longer characteristic time was reported. However, as shown in each panel of Figure 11, for fitting indexes higher than 0.65, there remains room to discuss the periodic variation of VSCAT in the VLBI-CLP-Data.

Effects of the Earth's rotation at the VLBI sight
In Figure 12, the fitting indexes produced as a result of the FITW for the VLBI-CLP-Data and DRWP -CLP-Model are given for the period range of 2005 to 2500 s. The results of the fitting indexes are clearly higher than those produced for the no VSCAT assumption for the closure phase. Though there are peaks of relatively high fitting indexes with periods of 2050, 2105, and 2200 s (0.70 and 0.65, respectively), the principal period of 2150 that has been confirmed as the period of the VSCAT for the flux density of the radiated 1.3 mm wavelength radio waves at SgrA* is a remarkable dip point. This evidence seems to show a contradiction between the flux density and closure phase in VSCATs. However, we found that the 2150 s periodic variation is still the
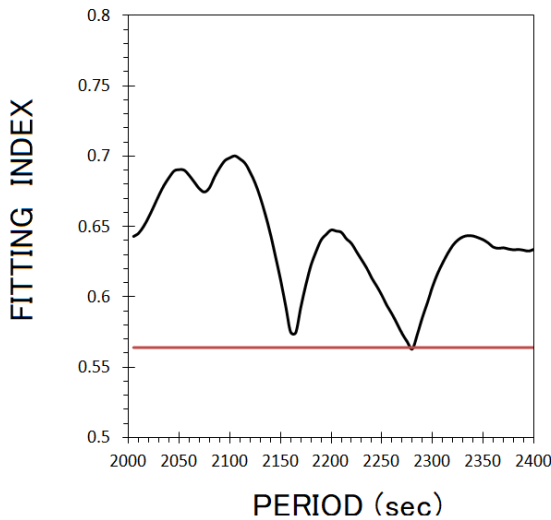

Figure 12: The fitting indexes of the FITW for the VLBI-CLP-Data and DRWP-CLP-Model for the period range of 2005 to 2500 s. The peak portion of the Fitting Index shifted from 2150 s to a range of 2050-2105 s due to the rotation effects of the VLBI sight. The red line is the index of the no VSCAT assumption for the closure phase.

principal intrinsic rotation period ; that is, we understand that the time variation in the closure phase detected by the VLBI shows results relative to the sights which are rotating with the Earth [21] . The setting period of the DRWP -CLP-Model given by eq.(18) with the angular velocity $\Omega(= 2\pi/T_{orb})$ should be understood as to be observed by transformed to Ω_{det} by Earth's rotation where the VLBI triangle baselines are rotating with the angular velocity Ω_E as

$$\Omega_{det} = \Omega \pm \Omega_E . \qquad (19)$$

where the sign $\pm$ is decided by knowing the relative spin direction between the detectable closure phase and the orbiting motion of the SMBHB. The present FITW results show that for an orbiting period T_{orb} (= 2150 sec) and an Earth rotation period of 86400 s, the rotation period T_{det} of the detectable closure phase can be predicted to be 2097 s for the case with the + sign. Within the possible error limit, the resulting T_{det} coincides with the FITW results for the VLBI-CLP-Data and DRWP CLP Model that show gradual peaks in the fitting index at around 0.7 in the period range from 2095 to 2105 s (see Figure 12). Though future work is required to gain accurate statistics because of the extremely limited data available for the closure phase in the present VSCAT study, we can state that there is periodic variation in the structure at Sgr A*. This result supports the results of the VSCAT for the flux density, which can be attributed to the orbital motion of the SMBHB, as concluded from the DRWP observations.

Proof of Necessity of the Coincidence by the Fourier Transformation Method (PNCF)
Fourier transformation under the effects of the data sampling time window (DSTW)
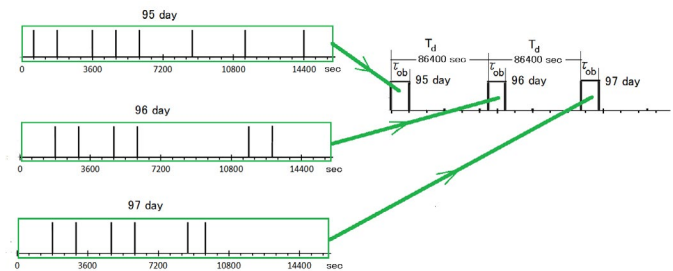
Figure 13: Depiction of the DSTW for the data published for 1.3 mm wavelength radio waves at Sgr A* by Fish et al [20] observed on April 5 (95th day),6 (96th day), and 7 (97th day). The DSTW consists of two hierarchies. The first is the time interval of 86400 s that separates observation days and the second is for observation intervals during periods of 10800 s, in average, during which 6 to 8 sampling time windows were set, as indicated by the black bars in green boxes.

Here, we describe the necessity of the coincidence in the FITW. The significant point is that the coincidence between the DRWP-Model and VLBI-Data for the VSCAT is not an accidental coincidence nor simply the external appearance. To investigate the underlying periodicity, therefore, we conducted FITW processes through the Fourier transformation for the time series of the data for both the VLBI-Data and DRWP-Model. In this section, we start with the expression of the data sampling time window (DSTW) throughout the entire three days of VLBI-Data collection. In Figure 13, the DSTW is displayed based on Table 1 corresponding to the FEHT paper. Using a sampling moment of t_m (m=1,2,3 ......, 20), we define the function of the DSTW $h(t, t_m)$ as a continuous function; that is, we express the sampled data point $f(t_m)$ for the observed

physical quantity results f(t) as

$$f(t_m) = f(t)h(t, t_m). \qquad (20)$$

When we set $h(t, t_m)$ as

$$h(t, t_m) = \begin{cases} \displaystyle\sum_{m=0}^{M} \delta(t - t_m) & \text{for } \eta T_d < t < \eta T_d + \tau_{ob} \\ 0 & \text{for } \eta T_d + \tau_{ob} < t < (\eta+1)T_d \end{cases} \qquad (21)$$

where T_d is a day separation and η is the intrger to indicate passing days after 95 day. The Fourier transformation of eq.(20) is expressed (details are described in Appendix D), as

$$D(\omega) = \frac{1}{2\pi(2T_d + \tau_{ob})} \int_{-\infty}^{\infty} F(\omega_b) \left\{ \sum_{\eta=0}^{2} \left[\sum_{m=M_\eta+1}^{M_{\eta+1}} A_\eta e^{-i(\omega-\omega_b)t_m^*} \right] e^{-i(\omega-\omega_b)\eta T_d} \right\} d\omega_b. \qquad (22)$$

where $F(\omega_b)$ is the Fourier transformation of f(t) for an idealistic data series, assuming that there is no effect of the DSTW; that is,

$$F(\omega_b) = \int_{-\infty}^{\infty} f(t)\, e^{-i\omega_b t} dt. \qquad (23)$$

This $F(\omega_b)$ represents ,all of three functions as for the case of idealistic data series for VLBI-Data, for the combination of the sinusoidal function of the DRWP-Model and the average of 160 cases of a random noise series to provide a flat (white noise) spectra. Using a function of the DRWP-Model to represent VSCAT, here, we considered f(t) = $\cos(\omega_0 t)$. The Fourier transformation corresponding to eq, (23) is given by

$$F(\omega_b) = \int_{-\infty}^{\infty} f(t)e^{-i\omega_b t}\, dt = \frac{1}{2}\int_{-\infty}^{\infty} \left(e^{i\omega_0 t} + e^{-i\omega_0 t}\right)e^{-i\omega_b t}\, dt \qquad (24)$$

Considering the relationship with the delta function, eq.(24) gives the expression

$$F(\omega_b) = \pi[\delta(\omega_b - \omega_0) + \delta(\omega_b + \omega_0)]. \qquad (25)$$

Then, the Fourier transformation of the DRWP-Model $D_{DMod}(\omega)$ corresponding to eq.(22) can be expressed as

$$D_{DMod}(\omega) = \frac{1}{2(2T_d + \tau_{ob})} \left\{ \sum_{\eta=0}^{2} \left[\sum_{m=M_\eta+1}^{M_{\eta+1}} A_\eta e^{-i(\omega-\omega_0)t_m^*} \right] e^{-i(\omega-\omega_0)\eta T_d} \right.$$
$$\left. + \sum_{\eta=0}^{2} \left[\sum_{m=M_\eta+1}^{M_{\eta+1}} A_\eta e^{-i(\omega+\omega_0)t_m^*} \right] e^{-i(\omega+\omega_0)\eta T_d} \right\}. \qquad (26)$$

where $t*$ is defined in relation to the DSTW t_m as $t_m^* = t_m - \eta\, T_d$ for the observation date η (= 0 for the first day ,95 and 2 for the last day, 97); T_d and τ_{ob} are the time lengths for a day (86400 s) in seconds; and the observation interval for each observation day are determined to be 3 h (10800 s) by adjusting the final rest time for each observation day. It should be noted that we use a time series t_m^* consisting of random intervals.in general, between each time interval, $t_{m+1}^*-t_m^*$. Contrary to the general time interval , we consider a time series with a constant interval T_I by introducing a new function S(ω-ω_0) ; that is

$$\frac{Z(\omega - \omega_0)}{\sum_{m=1}^{M_3} e^{[-i(\omega-\omega_0)mT_I]}} = S(\omega - \omega_0). \qquad (27)$$

where

$$Z(\omega - \omega_b) = \sum_{m=1}^{M_3} e^{-i(\omega - \omega_0)t_m} .\qquad(28)$$

Then, as described in Appendix D, we obtained the following results for $D_{DMod}(\omega)$:

$$D_{DMod}(\omega) =$$

$$\frac{1}{2(2T_d + \tau_{ob})}\left\{\frac{sin\{[(M_s + 1)/2](\omega - \omega_0)T_I\}}{M_s \cdot (\omega - \omega_0)(T_I/2)} e^{-i(\omega - \omega_0)(M_3/2)T_I}\right.$$

$$\left.\times\ S(\omega - \omega_0)\{2cos[(\omega - \omega_0)T_d] + 1\}e^{-i(\omega - \omega_0)T_d}\right\}.\quad(29)$$

where M_s is the DSTW number adjusted to be $\tau_{0b} = M_s T_I$.
Apart from the singular point at $\omega = \omega_0$, to express the VSCAT, the spectra given by eq.(26) can be expressed as function of ω by

$$D_{DMod}(\omega) = \frac{K_{DMod}}{2(2T_d + \tau_{ob})}\left[\sum_{m=1}^{M_s} e^{-i\omega m T_I}\ S(\omega - \omega_0)\right] \cdot [2cos[\omega T_d] + 1] \times e^{-i\omega T_d}\qquad(30)$$

where K_{DMod} is a constant that is expressed by

$$K_{DMod} = \sum_{m=1}^{M_3} 2cos(\omega_0 t_m) .\qquad(31)$$

Then, the absolute values of the spectra of the DRWP-Model, $|D_{DMod}(\omega)|$ are expressed by

$$|D_{DMod}(\omega)| = \frac{1}{2(2T_d + \tau_{ob})}\left\{\frac{sin\{[(M_s + 1)/2](\omega - \omega_0)T_I\}}{M_s \cdot (\omega - \omega_0)(T_I/2)}\right.$$

$$\left.\times\ S(\omega - \omega_0)|2cos[(\omega - \omega_0)T_d] + 1|\right\},\qquad(32)$$

for the range of ω close to ω_0; and

$$|D_{DMod}(\omega)| = \frac{K_{DMod}S(\omega - \omega_0)}{2(2T_d + \tau_{ob})}\sqrt{(D_{DMod}^R)^2 + (D_{DMod}^{Im})^2}\ |2cos[(\omega - \omega_0)T_d] + 1|,\qquad(33)$$

for the range of ω apart from ω_0. In eqs. (33) D^R_{DRod} and D^{Im}_{DRod} are defined as

$$D_{DMod}^R = \sum_{m=1}^{M_s} cos(\omega m T_I) ,\qquad(34)$$

and

$$D_{DMod}^{Im} = -\sum_{m=1}^{M_s} sin(\omega m T_I) .\qquad(35)$$

These results are characterized by the existence of ripple-like modulation in the full range of spectra multiplied by the form $\{2\cos[\omega T_d] + 1\}$, where the spectra show multiple local peaks at every frequency corresponding to $\omega = 2\pi\zeta/T_d$ (for the integer ζ), as given in Figure 16.

The spectra given by eqs.(32) and (33) are associated with complicated DSTW effects. To obtain pure VSCAT spectrum peaks with the DSTW effects removed, we use the Fourier transformation for a random noise time series that close up the features of the present DSTW by taking the average of 160 independent random noise time series. In the generation of the random noise data for the analysis, random numbers are distributed at completely synchronized times with the DSTW of the VLBI-Data that is applied to the data sampling of the DRWP-Model also. At t_m of the DSTW, the noise data $N_{Ran}(t_m)$ are generated for 160 independent cases using

$$N_{Ran}(t_m) = R_{Ran}(t_m) \times V_V + V_C. \qquad (36)$$

where $R_{Ran}(t_m)$ ($Ran = 1, 2, \ldots .160$) is a series of four-digit random numbers varying from 0 to 1, and V_V is the variation range, which was taken as 0.53 (J_y) to fit with the variation range of the VLBI-Data on days 95 and 96 and 0.32 (Jy) corresponding to the observations on day 97. Additionally, in eq.(36), the constant V_C is selected to be 1.69 (Jy) for days 95 and 96 and 2.62 (Jy) for day 97 to coincide with the VLBI-Data.

When there is no restriction on the sampling timing of $R_{Ran}(t)$, as in the DSTW, we are able to have the flat spectrum that could be expressed with a constant A:

$$A = \frac{1}{160} \sum_{Ran=1}^{160} \int_{-\infty}^{\infty} V_V R_{Ran}(t) e^{-i\omega t} dt. \qquad (37)$$

As described in Appendix D, also, by using this averaged spectrum, $F(\omega_b)$ can be considered to be a constant A that reflects the evidence of white noise. The Fourier transformation $D_{RAMD}(\omega)$ corresponding to $D(\omega)$ given by eq.(22) is then expressed by

$$D_{RAND}(\omega) = \frac{A}{2\pi(2T_d + \tau_{ob})} \left\{ \sum_{\eta=0}^{2} \sum_{m=M_\eta+1}^{M_{\eta+1}} A_\eta e^{-i\omega t_m^*} e^{i\omega\eta T_d} \right\} \times \frac{\int_{\omega_1}^{\omega_2} e^{i\omega_b t_m^*} d\omega_b}{\omega_2 - \omega_1} \qquad (38)$$

This relation gives the following result:

$$D_{RAND}(\omega) = \frac{K_{RAND}}{2\pi(2T_d + \tau_{ob})} \sum_{\eta=0}^{2} \sum_{m=M_\eta+1}^{M_{\eta+1}} A_\eta e^{-i\omega t_m^*} e^{i\omega\eta T_d} \qquad (39)$$

where K_{RAND} is a constant that, setting $A_0 = 1$, is given by

$$K_{RAND} = A \sum_{m=0}^{M_1} \frac{1}{i t_m^*(\omega_2 - \omega_1)} \cdot \left(e^{i\omega_2 t_m^*} - e^{i\omega_1 t_m^*} \right). \qquad (40)$$

Except for the frequency range with singular points that shows the existence of the VSCAT at $\omega = \omega_0$, the result given by eq.(37) is almost equal to the spectra of the DRWP-Model when the constant is changed from K_{DMod} to, K_{RAND} .Then, the absolute value of the RAND spectra can be expressed by

$$|D_{RAND}(\omega)| = \frac{K_{RAND} S(\omega - \omega_0)}{2(2T_d + \tau_{ob})} \sqrt{(D_{DMod}^R)^2 + (D_{DMod}^{Im})^2} \; |2\cos[\omega T_d] + 1|. \qquad (41)$$

Then, we can find the unknown value of $S(\omega - \omega_0) \cdot \sqrt{(D^R{}_{DMod})^2 + (D^{Im}{}_{DMod})^2}$ using the results of the numerical experiments $|D_{DAND}(\omega)|$ by averaging 160 cases of the random noise series. That is,

$$S(\omega - \omega_0) \cdot \sqrt{(D_{DMod}^R)^2 + (D_{DMod}^{Im})^2} \; = \; \frac{2(2T_d + \tau_{ob})|D_{DAND}(\omega)|}{|2\cos[\omega T_d] + 1| \cdot K_{RAND}}. \qquad (42)$$

Then, we can express $|D_{DMod}(\omega)|$ as

$$|D_{DMod}(\omega)| = \begin{cases} \dfrac{|D_{RAND}(\omega)|}{\sqrt{(D_{DMod}^R)^2 + (D_{DMod}^{Im})^2}} \dfrac{K_{DMod}}{K_{RAND}} \left\{ \dfrac{sin\{[(M_s+1)/2](\omega-\omega_0)T_I\}}{M_s \cdot (\omega-\omega_0)(T_I/2)} \cdot G(\omega) \right\} \\ \qquad \ldots\ldots\ldots\ldots. \text{for } \omega_0 - \Delta\omega < \omega < \omega_0 + \Delta\omega \\ \\ |D_{RAND}(\omega)| \dfrac{K_{DMod}}{K_{RAND}} \ldots\ldots\ldots \text{for } \omega_0 - \Delta\omega > \omega, \text{ or } \omega > \omega_0 + \Delta\omega \end{cases}$$

where
(43)

$$G(\omega) = |2\cos[(\omega-\omega_0)T_d] + 1|/|2\cos[\omega T_d] + 1|. \qquad (44)$$

If there are VSCATs that have potential periodicity in the VLBI-Data, we can apply the procedure to obtain an absolute value through the Fourier analyses applied to the DRWP-Model; that is, dividing the absolute value $|D_{VLBD}(\omega)|$ of the calculated Fourier transformed results by $|D_{RAND}(\omega)|$, for the VLBI-Data, we can search for the possible spectra peaks by removing the DSTW effects that naturally occurred during the time of the observations by FEHT. Thus, we compared $|D_{VLBD}(\omega)|/|D_{RAND}(\omega)|$ with
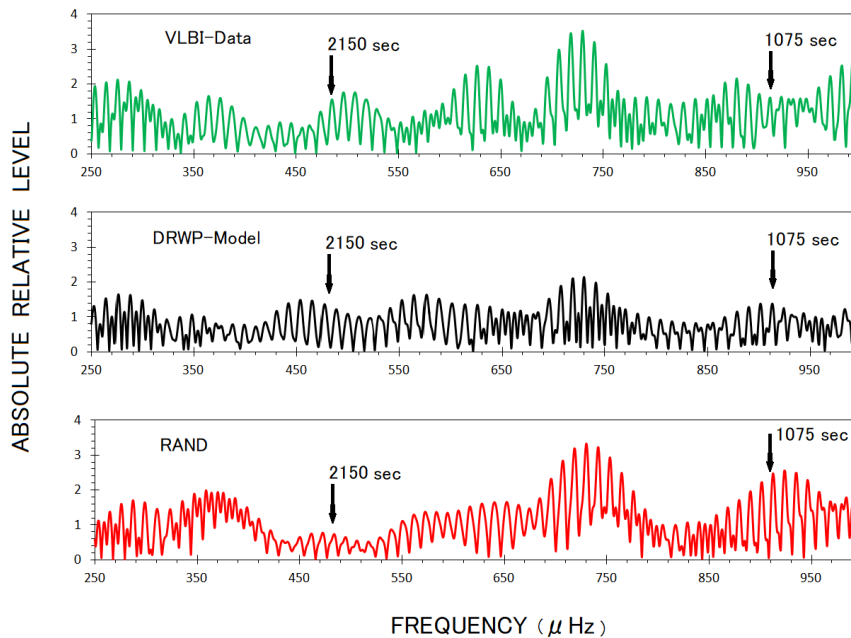

Figure 14: Absolute values of the results of the direct Fourier transformation $D_{VLBD}(\omega)|$, $|D_{DMod}(\omega)|$ and $|D_{RAND}(\omega)|$ corresponding, respectively, to the VLBI-Data (top panel), DRWP-Model (middle panel), and RAND (bottom panel). The abscissa indicates the frequency expressed in µHz. We use the relation $f \cdot T = 10^6$ to translate the frequency f in µHz with the period T in s, vice versa.. In all panels, frequencies corresponding to the two principal spectra peaks at T=1075 s and 2150 s are indicated. In all panels, the spectra are associated with remarkable ripples whose repeating frequency intervals are around 11.6 μ Hz and with half of that in several portions (see Appendix E).

$|D_{DMod}(\omega)|/|D_{RAND}(\omega)|$ to verify the existence of the peaks in the spectra at the same frequencies (periods inversely) by removing the DSTW (data sampling time window) effects.

Numerical Results of the Fourier Transformation with DSTW effects

In Figure 14, the direct Fourier-transformed results $|D_{VLBD}(\omega)|$, $|D_{DMod}(\omega)|$ and $|D_{RAND}(\omega)|$ corresponding to the VLBI-Data, DRWP-Model, and RAND are displayed in the top, middle and bottom panels, respectively. In this figure, the abscissa is indicated by the frequency f in µHz . The transformation of the abscissa in the period of
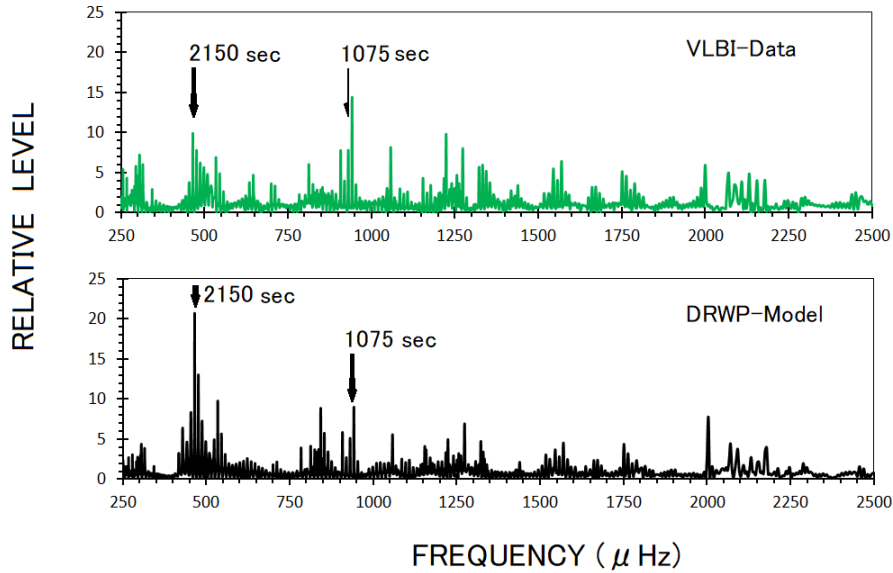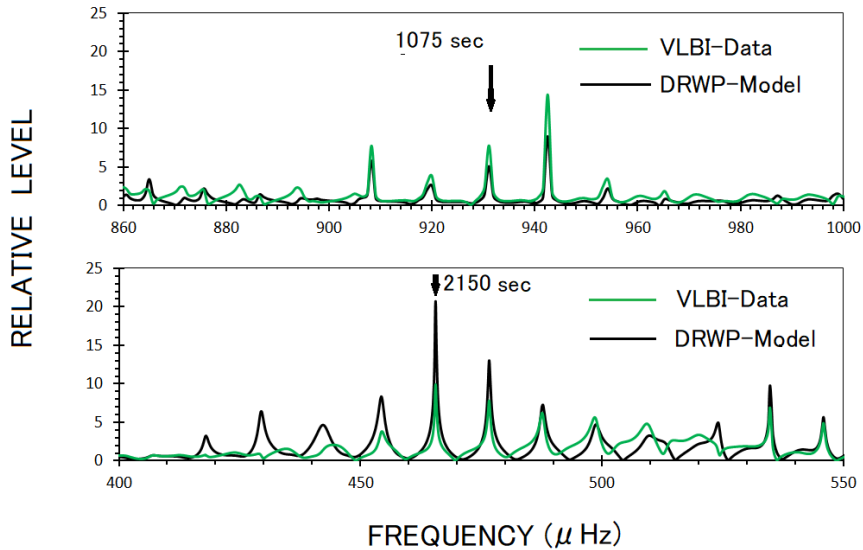
Figure 15: Spectra of the VLBI-Data and DRWP-Model with the effects of the DSTW removed through division with RAND (see eq. (46)) using $|D_{VLBD}(\omega)| / |DRAND(\omega)|$ (in the top panel) and $|D_{DMod}(\omega)| / |D_{RAND}(\omega)|$ (in the bottom panel). The results of the direct Fourier transformation (Figure 14) show that the DSTW effects were cleaned up, and peaks at 930 µHz (1075 s) and 465 µHz (2150 s) are indicated, coinciding with the results of the VLBI-Data and DRWP-Model associated with several minor peaks corresponding to the frequency $1/t*$. The modulation of the surrounding peaks of the local frequency range was newly formed due to division by $|DRAND(\omega)|$ through the effects of the function $G(\omega)$ (see eq.(47)).

T s is made using a mutual relation at $f \cdot T = 10^6$. In all spectra given in the top to bottom panels, a similar tendency of complex features can be seen. This is characterized by the case of the RAND spectra, suggesting common effects of the DSTW. Whole spectra are clearly modulated by the DSTW of a day length observation periods, as theoretically predicted in Appendixes D and E. The appearance of modulation in the VLBI-Data spectra and DRPW-Model is evidence to realize the theoretical background in terms of setting the concept of DSTW and righteousness focusing the average of multiple random noise series to remove the DSTW effects.

Numerical Results of the Fourier Transformation by Removing DSTW Effects

The numerical results for $|D_{VLBD}(\omega)|/|D_{RAND}(\omega)|$ and $|D_{DMod}(\omega)|/|D_{RAND}(\omega)|$ displayed in Figure 15 where spectra in the frequency range of 250 to 2500 µHz are

Figure 16: Close up of the Fourier Transformation results (with the DSTW effects removed) for the VLBI-Data and DRWP-Model overwrapped together in the top panel for the 930 µHz peak (1075 s period) and the bottom panel for the 465 µHz peak (2150 s period). The oscillating subpeaks associated with the principal spectra peaks in both panels are explained in Appendix D. Modulation with the feature of oscillations takes place with the local maxima frequencies at every $1/T_d \ Hz \approx 11.6 \ \mu Hz$. In the case of a period of 1075 s, the

maximum peak is shifted one step (≈ 11.6 µHz) to a frequency higher than 930.2 µHz being subjected to DSTW modulation. The real maximum peak is modified by the DSTW (see G(ω) given in eq.(44)), as confirmed by the complete coincidence with the DRWP-Model, whose original center peak is given at 930.232 µHz .

indicated for VLBI-Data (top panel) and DRWP-Model (bottom panel) divided by |D$_{RAND}$(ω)| to remove the DSTW. The complicated features observed in the results of the direct Fourier transformation (Figure 14) are cleaned up so that principal spectra peaks are revealed at 930 µHz (1075 s) and 465 µHz (2150 s). These are associated with several minor peaks corresponding to a frequency of $1/t*$ because the absolute level of the spectra are determined through mathematical manipulation of the square root to detect the absolute values. Through the process of taking the square root, spectra peaks are generated in addition to the original peeks, though the original peaks are never lost. After cleaning up the modulation feature of the spectra, further modulation are remained required in the local frequency ranges surrounding the peaks, as shown in Figure 15. The remainder of the modulation effects can be understood through eq.(44) (see Appendix D, also), where the origin of the modulation effects are indicated by G(ω) . Except for the case of $\omega_0 = 0$, modulation takes place as oscillations in the spectra with recurrence of peaks at frequencies , every $1/T_d$ Hz.

Figure 16 shows the close up feature of the principal peaks of the spectra at around 930 µHz (1075 sec) and 465 µHz (2150sec) for VLBI-Data and DRWP-Model. overwrapping together in these resultant spectra; we confirm, here, the complete coincidence of the spectra for the VLBI-Data and DRWP-Model. In the case of spectra with a period of 1075 s, the maximum peak is shifted one step (≈ 11.6 µHz) to a frequency higher than 930.2 µHz being subjected to DSTW modulation. We did not select this maximum peak of 940.4 µHz, as the principal peak because the modulation of the DSTW on the principal peaks is apparent, as confirmed by the evidence of complete coincidence of peaks of spectra between

VLBI data and the DRWP-Model; that is, the DRWP-Model is basically constructed with spectra with peaks at 930 µHz (1075 s) and 465 µHz (2150 s). That is, we conclude that by the Fourier analysis with data sampling through the DSTW, the highest peak is shifted from 930.2 µHz to 940.4 µHz, completely coinciding with the case of VLBI-Data.

The existence of a peak at 465.1 µHz (T=2150 s), together with one at 930.2 µHz (T=1075 s), in the VLBI-Data and DPRW-Model is confirmation of the necessity of the existence of the VSCAT in VLBI-Data coinciding with the DPRW-Model that is constructed based on the results of the SMBHB [23].

Discussion
Effects of data sampling time window (DSTW) on the Direct Fitting of the DRWP-Model
The importance of the DSTW effects on the present FITW are described in Sec PNCF. in relation to the coincidence between the VIBI-Data and DRWP-Model in terms of the transformed frequency space. Here, we provide a further discussion of the effects of the DSTW on the direct fitting (fitting in the time-space) between the VIBI-Data and DRWP-Model to give further confirmation of the existence of VSCAT in the VLBI-Data that coincides with the DRWP-Model..

When function f(t_m) is expressed with f(t) and h(t, t_m) (see eq. (20)) we can rewrite h(t, t_m) functions with inverse Fourier transformation as described in Appendix C by eq.(C4) using angular frequency $\omega = 2\pi/T$ for the period T; that is,

$$h(t, t_m) = \int_{-\infty}^{\infty} \left\{ cos\left[\frac{2\pi}{T}(t - t_m)\right] + i \cdot sin\left[\frac{2\pi}{T}(t - t_m)\right] \right\} \frac{dT}{T^2}. \text{for} 1 < m < M \quad (45)$$

The integration in eq.(45), that is subjected to the wide range of the period T makes the contribution from above two terms which approximately vanish except for the case $t \approx t_m$; then we can approximate eq.(45) to the following

$$h(t, t_m) \approx H_c cos\left[\frac{2\pi}{T_s}(t - t_m)\right] ; \text{for} 1 < m < M \quad (46)$$

where H_c is a constant whose value is decided to fit the result of integration in eq.(45); and in DSTW we set a constant interval T_s.

For understanding the coupling effect of DSTW, we select a simple case for f(t) ; that is f(t) = $A_m cos(2\pi t / T_{ob})$. Then, it follows from eq.(20) that (see Appendix C)

$$f(t_m) = \frac{AH_c}{2} cos\left(\frac{2\pi t_m}{T_{ob}}\right) \cdot cos\left[\frac{2\pi}{T}(t_m - mT_S)\right]; \text{ for } 1 < m < M \qquad (47)$$

As described in Appendix C also, we have relation, by rewriting eq.(49) , with selection of $T = T_S$ as

$$f(t_m) = \frac{AH_c}{4}\left\{cos\left[2\pi\left(\frac{1}{T_S} + \frac{1}{T_{ob}}\right)t_m\right] + cos\left[2\pi\left(\frac{1}{T_S} - \frac{1}{T_{ob}}\right)t_m\right]\right\}. \text{ for } 1 < m < M \qquad (48)$$

In eq.(48) we see the feature of the modulation of DSTW which modify the original data series $A cos[2\pi(1/T_{ob})t_m]$ with respect to the period T_{ob} to the data form given by two terms with the period ,$T_{ob}T_S/(T_{ob} + T_S)$ and $T_{ob}T_S/(T_{ob} - T_S)$.

In Figure 17, fitting indexes for setting a wide period range in the DRWP-Model compared with the VLBI-Data are given for the maximum values in each period; that is, with respect to each period from 1500 to 3950 s, for cases with an eclipse parameter of n=2, 4 and 8, (indicates the eclipse feature, see the bottom diagrams in

Figure 4), the maximum I_c (see eq.(17)) is investigated with the initial phase of the DRWP-Model set at 11:00 h (UT) on the 95th day by sweeping the entire range from 0 to 360 degrees with 2.5 degree steps. Two fitting index peaks I_c are observed for all three cases of n; the first peak appears at the period of $T_{1st}(=2150)$ s and the second appears at the period of $T_{2nd}(=2950)$ s. As shown in all three diagrams, the first peak correlated within the period range predicted by the DRWP observations (P.R. given in the diagrams). Though
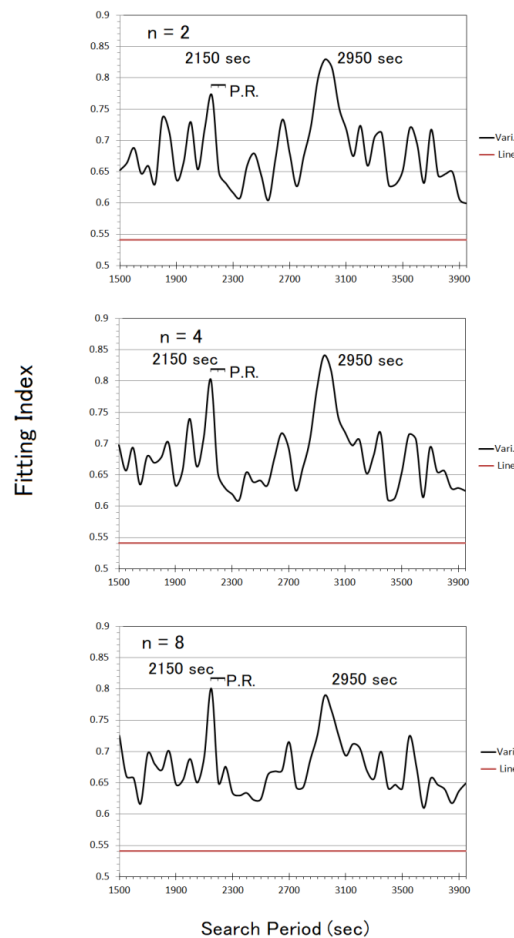
Figure 17: Maximum fitting indexes (Vari) for the three DRWP-Models with eclipse function parameters of n=2, 4, and 8 at each period in the range of 1500 to 3950 s. For values greater than 2500 s, the peak of the maximum fitting index is shown at a period of 2950 s. This is caused by the coupling of the principal period, 2150 s (P.R.), with the DSTW, which can be estimated as an interval of 1243 s. The red line (Line) shows the fitting index for the case with the assumption of no VSCAT.

the second peak is further out of the predicted rage, we observe that the second peak occurs as result of the coupling with the DSTW, and it becomes clear that this peak is intimately related to the first peak period. Regarding the argument in eq.(48) where we have described the effect of DSWT , the occurrence of the second peak at $\omega_{2nd} = 2\pi/T_{2nd}$, is related to the first peak at $\omega_{1st} = 2\pi/T_{1st}$ by

$$\frac{1}{T_{2nd}} = \frac{1}{T_s} - \frac{1}{T_{1st}}. \quad (49)$$
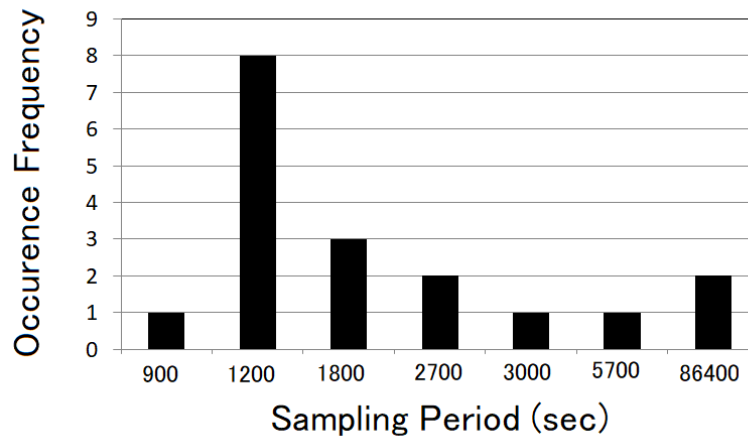
Figure 18: Histogram showing the interval $t_{m+1} - t_m$ of the DSTW for all three days from 11:00 h(UT) on the 95th day to 14:00 h on the 97th day.

where T_s is the one of representative sampling period. The sampling period T_s of the VLBI-Data is not fixed to a single value; therefore, the effect of the sampling period shows complicated features. However, we observe two clear tendency, as given in Figure 18. The first is the data sampling period around 1200 s. The 8 sampled data points possibly affect as the constant sampling time window with a period around 1200s. By assuming the second peak was a shadow of the first peak, we deduced the possible average period of the sampling, from eq.(49) as

$$T_S = \frac{T_{1st} \cdot T_{2nd}}{T_{2nd} + T_{1st}} = \frac{2150 \times 2950}{2950 + 2150} = 1243 \ (sec) \quad (50)$$

We can accept these results as possible values within a considerable error range around 1200 s, which can be considered one of the dominant values of the DSTW. Then we consider that the occurrence of the first peak represents the direct manifestation of the period connected to underlying physical processes predicted by DRWP observations. By referring to the results of the Fourier analysis given in Sec PNCF, we can confirm this context; that is, while we observe the complete existence of the spectra peak at 465 µHz corresponding to a period 2150 s (Figure 15), there is no signature of the peak at 339.0 µHz, corresponding to a period of 2950 s.

The second tendency of DSTW that we can find from the histogram, in Figure 18 ,is randomness for 11 sampling intervals whose periods are spread for over a fairly wide range, from 3000 sec to 86400. Due to this randomness of DSTW no remarkable T_S appears to bother the sampling period for the detection of the first peak at 2150 sec,
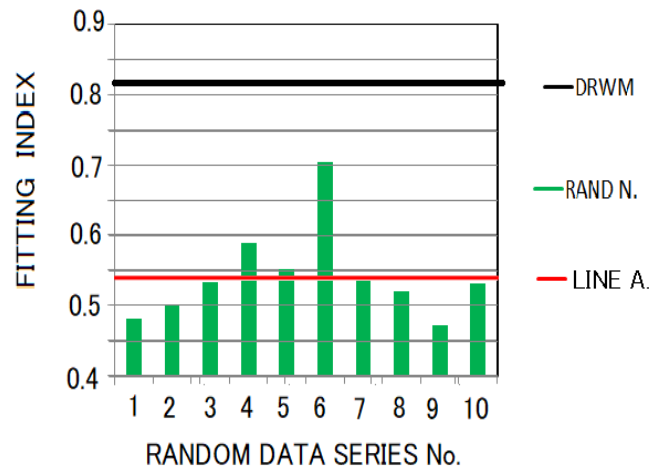
Figure 19: Examples of fitting results for 10 random noise series with the same DSTW for the VLBI-Data and DRWP-Model. The evaluation indexes are lower than the constant assumption of no VSCAT (LINE A) for 7 cases, but case No.6 suggests the existence of accidental coincidence, although the fitting index is clearly lower than in the case of maximum coincidence (DRWM)

In Figure 19, the fitting results for the DRWP-Model with n=4 that is applied to the FITW with the VLBI-Data resulting evaluation index of 0.811 (see Figure 9.) are indicated with the fitting results for10 sets of random noise data. As expected, the fitting results show an apparently less coincidence. For the majority of cases of random noise, the fitting status are worse than for the case of stationary assumption (given by LINE A.). There is, however, one case, No.6, which is determined to be an accidental coincidence, although we do not accept its fit, because the evaluation index was still clearly lower than 0.8.

These numerical experiments with random noises suggest, however, that if we rely only on the time-space fitting between VLBI-Data and DRWP-Model, there would occur accidental coincidences in parallel to real coincidences. From this point of view, it is essential to investigate the potential periodicity of VSCAT using the Fourier transformation as carried out in Sec PNCF.

Robust repetition phase
In addition to the confirmation of the necessity of the coincidence in FITW that has already been described, we are further able to confirm the extremely robust characteristics of the time variation in VSCAT by keeping the phase given at the starting time of 11:00 h (UT) on the 95th day .As we see in Figures 7 and 8, the coincidences take place at extremely critical moments in the variation in the DRWP-Model, indicating steep variation in the eclipse effects, as indicated for the case of the 97th day after 12:00 h (UT), for example, when the time passed are more than 170,000 s after setting the initial phase angle. For the datum sampled at this timing it is allowed only ±30 sec to obtain an fitting index value of 0.9 as achieved by this datum ; we are required accurate stability with a blurring rate of less than 1.8×10^{-4}. That is, we cannot

expect the continuation of such highly accurate repetition, except for in the orbiting motion of the celestial body.

On generation of the gravitational wave from the SMBHB
In terms of accepting the results of the present FITW for the VLBI-Data and VLBI-CLP-Data, it could be argued that the result would be contradictory to the possible generation of gravitational waves from the binary of compact celestial objects such as neutron stars and black holes. Due to radiation of the intense gravitational wave energy, it is impossible to exist for an extreme system, such as that described in the present work. That is, if we apply the Landau Lifshitz equation [28] for the variation of the distance of the binary with parameter that we have indicated in Figure 2, two bodies merge within 8 hours.

However, when we reconsider the current paradigm for gravitational waves from compact objects, there still remains a wide area of investigation. These are 1) Has the assumption that the observed gravitational waves are sourced by star mass to the medium mass black hole binaries been proved experimentally? 2) Is there any evidence of the merging of the supermassive black hole that involves confirmation via observations of the gravitational waves? We are at the point of considering that there is a possibility to quest for the case of no gravitational waves from the SMBHB. The present theories regarding gravitational waves from black holes concern stellar mass to intermediate mass black holes, but the theories regarding the generation of gravitational waves from the SMBH are deferred for future studies

Conclusion
The millimeter wavelength VLBI observations in the EHT project are based on the firm results of Fish et al, revealed a promising

direction for research on the formation of the coherent radio wave flux density related to the black hole shadow at Sgr A*. However, because of the unexpected time variation in the VLBI data for sources within a few Schwartzschild radii, the formation of a visualized radio wave image of Sgr A* has been delayed three years after the publication of the image of M87* which were observed almost the same periods in April 2017. Explanations for the time variation and the persistence of the time variation in the structure within 50 μas have been mostly related to movements of the turbulent plasma, whose dense electrons interrupt stable propagation of the emitted mm wavelength radio waves. Under such circumstance, the EHTC forced to release the visualized image of the shadow of SgrA*. Unfortunately from the stand point of smooth progress of the astrophysics, the released image contains double defects; one is the structural defects caused by misevaluation of initial image for the step processes of hybrid mapping and other is caused by misevaluation of time varying nature of the mm wavelength radio wave emissions. Without relation to the such recently occurred issue of defects, the studies of sources around SgrA* continued firm progresses after 2009, by 1.3 mm wavelength VLBI that approaches to the source size of the event horizon of SgrA*.

Independently of the high-frequency radio wave observation tasks, we have considered the radio wave radiation from the closest regions of the event horizon of the supermassive Kerr black holes in the decameter wavelength range, which is generated as whistler mode waves associated with the magnetized plasma environment. We reviewed the results of decameter radio wave research,; after tunneling through the dense plasma region (where the propagating wave frequency f is less than the local plasma frequency f_p) , the whistler mode waves are converted into ordinary mode radio waves, which can propagate through the galactic space until arriving at the observation point at the Earth's surface in the form of pulses reflecting the spin and orbital motion of the sources, as deciphered from the observed complexed spectra of the pulse periods. By analyzing pulse periods with the regular FFT method, information about the supermassive black holes has been clarified. The black holes at Sgr A* consist of the binary with masses of 2.27 million $M_\odot$ (called temporarily Gaa) and 1.94 million $M_\odot$ (called Gab) orbiting with a period of 2200 ± 50 sec. The radii of the orbits of Gaa and Gab are 1.89×10^7km and 2.21×10^7km , respectively. The range covered by the orbits of 4.10×10^7km corresponds to 3.25 R_{ss} for the currently believed Shwarzschild radius R_{ss} of the single black hole with a mass of about $4.28 \times 10^6 M_\odot$. The supermassive black holes are orbiting with speeds of 0.18c and 0.21c for Gaa and Gab, respectively.

In the present paper, we concern with time variations detected at Sgr A* using the 1.3 mm wavelength VLBI observations of the Fish et al group that affected to start of EHT group, especially those presented in the initial studies by Fish et al regarding variation with short characteristic time (VSCAT) of around a few ten minutes, although the authors did not explicitly point this out, except for longer time scales in the order of days. Our concern is whether the time variation in the flux density has the same period of around 2200 ± 50 sec. as the manifestation of the orbital motion of the SMBHB.

For the purpose of the comparison with the flux density of 1.3 mm wavelength VLBI data (VLBI-Data) for the VSCAT, a model with time variation coinciding with the orbital motion of the SMBHB has been constructed. For this, we have employed essential parameters obtained by observations of the decameter radio wave pulses (DRWP). Considering the difference in the total mass of the supermassive black hole based on the orbital motion, $4.21 \times 10^6 M_\odot$ and $4.28 \times 10^6 M_\odot$, as deduced by star tracking studies, the tilt of the orbital plane from the looking direction from the earth are deduced to be 6°; that is, we are observing the eclipse of the SMBHB. Using the constructed time variation model (DRWP-Model), the comparison of the VLBI data and DRWP-Model has been carried out focusing on VSCAT. To make the evaluation of the fitting objective, a statistical index to evaluate the significance of the fitting state is defined with a Gaussian statistic function which indicates the unity when both data completely coincide.

By fitting works (FITW) between DRWP-Model and the VLBI-Data from the results published by Fish et al (observed from May 5 to 7 corresponding to days 95, 96 and 97,respectively in 2009), the existence of VSCAT has been concluded. In the original paper, the authors pointed out the variation in the observed flux density on a daily basis between the previous two days (days 95 and 96) and the data observed on day 97, indicating variation from 2.07 Jy on days 95 and 96 days to 2.4 Jy on day 97 in term of the median value. By overwrapping on the variation in the daily time scale as a variation in the background luminosity, we further conclude that there exists VSCAT with definite periodicity at a period of 2150 ± 2.5s with a fitting index of 0.81, which is remarkably closer to unity than the fitting index of 0.54, which can be considered as the threshold for assuming a constant flux density through out the entire three days; the resultant period is within the period range of 2200 ± 50 s predicted by the DRWP observation study, though it is close to the lowest limit. To verify that the fitting of the DRWP-Model to VLBI-Data is not accidental, the necessity of the resultant periodicity of the VSCAT has been investigated by applying the Fourier transformation. The results have revealed the significance of the data sampling time window (DSTW) with respective to the periods of the observing phenomena. By taking 160 cases of the random noise utilized to detect the Fourier-transformed DSTW, the coupling effects of DSTW with the intrinsic time-varying spectra of the observing phenomena are determined. After discrimination of the effects of the DSTW, it is concluded that the VSCAT in the VLBI-Data has intrinsic time variation with a period of at 2150 ± 2.5s for the data published by Fish et al for three days in May 2009.

In addition to the intensity of the flux density from the compact area of SgrA*, the significance of the non-zero closure phases of the VLBI triangle system were pointed out by the authors; within limited amount of usable data for the FITW, we tried to investigate

the coincidence with the closure phase data of VLBI-data (VLBI-CLP-Data) and the simplified model based on the orbital motion of the SMBHB (DRWP-CLP-Model), which consists of an aligned bar of two SMBHBs observed from Earth with a line of sight that is almost parallel to the orbital plane of the SMBHB. Though the published data with accurate observation timing are limited to only 10 data points within a day on day 93 in 2009, the maximum fitting indexes in the FITW show values in the range around 0.7 in the maximum region in the period from 2090 to 2105 s, suggesting that there is rotation of the structure at the Sgr A* with a proper rotation period of 2150 s that is shifted to around 2100 s due to the effect of the Earth's rotation. However, because of the limited data points for the closure phase, confirmation is deferred to future study.

Through the results of the FITW, we conclude that, in the data reported by the 1.3 mm wavelength VLBI for compact sources within a few Schwartzschild radii, the variation in the short characteristic time scale exists not only as a random scatter feature, but also as a long-persisting periodic variation with a period of $2150 \pm 2,5$ s. This coincides with the prediction of the existence of the super-massive black hole binary at Sgr A* with orbits expanding to 4.10×10^7km concluded by the DRWP work. To accept this conclusion, however, we are required a paradigm shift regarding the generation of gravitational waves from black holes if we are to state that all black holes radiate gravitation waves. As future work, we will study the generation of gravitational waves for the case of the SMBHB questing for cases of no gravitational wave from SMBHB..

References
1. Akiyama, K., Alberdi, A., Alef, W., Algaba, J. C., Anantua, R., Asada, K., ... & Martí-Vidal, I. (2022). First Sagittarius A* Event Horizon Telescope Results. I. The Shadow of the Supermassive Black Hole in the Center of the Milky Way. The Astrophysical Journal Letters, 930(2), L12.
2. Akiyama, K., Alberdi, A., Alef, W., Algaba, J. C., Anantua, R., Asada, K., ... & Martí-Vidal, I. (2022). First Sagittarius A* Event Horizon Telescope Results. II. EHT and Multiwavelength Observations, Data Processing, and Calibration. The Astrophysical Journal Letters, 930(2), L13.
3. Akiyama, K., Alberdi, A., Alef, W., Algaba, J. C., Anantua, R., Asada, K., ... & Martí-Vidal, I. (2022). First Sagittarius A* Event Horizon Telescope Results. III. Imaging of the Galactic Center Supermassive Black Hole. The Astrophysical Journal Letters, 930(2), L14.
4. Akiyama, K., Alberdi, A., Alef, W., Algaba, J. C., Anantua, R., Asada, K., ... & Martí-Vidal, I. (2022). First Sagittarius A* Event Horizon Telescope Results. IV. Variability, Morphology, and Black Hole Mass. The Astrophysical Journal Letters, 930(2), L15.
5. Event Horizon Telescope Collaboration; Akiyama, K.; Alberdi, A. and 272 more, First Sagittarius A* Event Horizon Telescope Results. V. Testing Astrophysical Models of the Galactic Center Black Hole, Astrophys. J. Lett. 2022, 930; L16.
6. Akiyama, K., Alberdi, A., Alef, W., Algaba, J. C., Anantua, R., Asada, K., ... & Martí-Vidal, I. (2022). First Sagittarius A* Event Horizon Telescope Results. VI. Testing the Black Hole Metric. The Astrophysical Journal Letters, 930(2), L17.
7. Akiyama, K., Alberdi, A., Alef, W., Asada, K., & AZULY, R. (2019). First M87 event horizon telescope results. I. The shadow of the supermassive black hole. Astrophys. J. Lett, 875(1), L1.
8. Akiyama, K., Alberdi, A., Alef, W., Asada, K., Azulay, R., Baczko, A. K., ... & Ramakrishnan, V. (2019). First M87 event horizon telescope results. III. Data processing and calibration. The Astrophysical Journal Letters, 875(1), L3.
9. Akiyama, K., Alberdi, A., Alef, W., Asada, K., Azulay, R., Baczko, A. K., ... & Ramakrishnan, V. (2019). First M87 event horizon telescope results. III. Data processing and calibration. The Astrophysical Journal Letters, 875(1), L3.
10. Akiyama, K., Alberdi, A., Alef, W., Asada, K., Azulay, R., Baczko, A. K., ... & Ramakrishnan, V. (2019). First M87 event horizon telescope results. IV. Imaging the central supermassive black hole. The Astrophysical Journal Letters, 875(1), L4.
11. Akiyama, K., Alberdi, A., Alef, W., Asada, K., Azulay, R., Baczko, A. K., ... & Rao, R. (2019). First M87 event horizon telescope results. V. Physical origin of the asymmetric ring. The Astrophysical Journal Letters, 875(1), L5.
12. Akiyama, K., Alberdi, A., Alef, W., Asada, K., Azulay, R., Baczko, A. K., ... & Rao, R. (2019). First M87 event horizon telescope results. VI. The shadow and mass of the central black hole. The Astrophysical Journal Letters, 875(1), L6.
13. Fish, V. L., Johnson, M. D., Lu, R. S., Doeleman, S. S., Bouman, K. L., Zoran, D., ... & Vertatschitsch, L. E. (2014). Imaging an event horizon: mitigation of scattering toward Sagittarius A. The Astrophysical Journal, 795(2), 134.
14. EHT Collaboration, Imaging Re-analyses of EHT data https://eventhorizontelescope.org/blog/imaging-reanalyses-eht-data
15. Miyoshi, M., Kato, Y., & Makino, J. (2022). The jet and resolved features of the central supermassive black hole of M 87 observed with EHT. arXiv preprint arXiv:2205.04623.
16. Zhao, J. H., Young, K. H., Herrnstein, R. M., Ho, P. T. P., Tsutsumi, T., Lo, K. Y., ... & Bower, G. C. (2003). Variability of Sagittarius A*: Flares at 1 millimeter. The Astrophysical

Journal, 586(1), L29.

17. Miyazaki, A., Tsutsumi, T., & Tsuboi, M. (2004). Intraday variation of Sagittarius A* at short millimeter wavelengths. The Astrophysical Journal, 611(2), L97.

18. Eckart, A., Schödel, R., García-Marín, M., Witzel, G., Weiss, A., Baganoff, F. K., ... & Zensus, J. A. (2008). Simultaneous NIR/sub-mm observation of flare emission from Sagittarius A. Astronomy & Astrophysics, 492(2), 337-344.

19. Marrone, D. P., Baganoff, F. K., Morris, M. R., Moran, J. M., Ghez, A. M., Hornstein, S. D., ... & Bower, G. C. (2008). An x-ray, infrared, and submillimeter flare of Sagittarius A. The Astrophysical Journal, 682(1), 373.

20. Fish, V. L., Doeleman, S. S., Beaudoin, C., Blundell, R., Bolin, D. E., Bower, G. C., ... & Ziurys, L. M. (2011). 1.3 mm wavelength VLBI of Sagittarius A*: Detection of time-variable emission on event horizon scales. The Astrophysical Journal Letters, 727(2), L36.

21. Fish, V. L., Johnson, M. D., Doeleman, S. S., Broderick, A. E., Psaltis, D., Lu, R. S., ... & Ziurys, L. M. (2016). Persistent asymmetric structure of Sagittarius A* on event horizon scales. The Astrophysical Journal, 820(2), 90.

22. Miyoshi, M., Shen, Z. Q., Oyama, T., Takahashi, R., & Kato, Y. (2011). Oscillation phenomena in the disk around the massive black hole Sagittarius A. Publications of the Astronomical Society of Japan, 63(5), 1093-1116.

23. Oya, H. (2019). Detection of Decameter Radio Wave Pulses from the Center Part of Our Galaxy Suggesting Sources at Rotating Super Massive Black Hole Binary. TERRAPUB e-Library, 1-50. http://hdl.handle.net/10097/00126480

24. Gillessen, S., Plewa, P. M., Eisenhauer, F., Sari, R. E., Waisberg, I., Habibi, M., ... & Genzel, R. (2017). An update on monitoring stellar orbits in the galactic center. The Astrophysical Journal, 837(1), 30.

25. Abdujabbarov, A., Atamurotov, F., Kucukakca, Y., Ahmedov, B., & Camci, U. (2013). Shadow of Kerr-Taub-NUT black hole. Astrophysics and Space Science, 344(2), 429-435.

26. Gralla, S. E., Holz, D. E., & Wald, R. M. (2019). Black hole shadows, photon rings, and lensing rings. Physical Review D, 100(2), 024018.

27. Eckart, A., Zajacek, M., Parsa, M., Fazeli, E. H. N., Busch, G., Shahzamanian, B., ... & Kamali, F. (2018). The Multifrequency Behavior of Sagittarius A. arXiv preprint arXiv:1806.00284.

28. Landau, L. D., & Lifshitz, E. M. (1967). The Classical Theory of Fields Third Revised English Edition Course of Theoretical Physics.

Appendix A

To deduce the masses of the SMBHB, Newtonian dynamics is applied with circular orbit approximation. By applying the Kepler relation for the Gaa and Gab BHs with masses of M_{Gaa} and M_{Gab}, respectively, we obtained the relation

$$M_{Gaa} + M_{Gab} = \frac{1}{G}\left(\frac{2\pi}{T_{0b}}\right)^2 (R_{oba} + R_{obb})^3 \qquad (A1)$$

where G, and T_{0b} are the gravity constant and orbiting period; R_{oba} and R_{obb} are the orbit radii of the BHs Gaa and Gab, respectively. In the original paper [23], the orbital velocities of Gaa and Gab were deduced from the frequency modulation effects on the spectra, showing the spin periods of Gaa and Gab, to be 0.18c and 0.21c ,respectively. The orbital velocity v_{obi} ($i = a$ for Gaa; $i = b$ for Gab) on the orbit with an inclination of θ_I is expressed with the velocity component v_{si} in the line of sight as

$$v_{obi} = \frac{v_{si}}{sin\theta_I} . \qquad (A2)$$

Considering that the orbital velocity v_{obi} can be rewritten using the orbit radius R_{obi} as

$$v_{obi} = \frac{2\pi}{T_{0b}} R_{obi}, \qquad (A3)$$

then eq.(A1) can be written by

$$M_{Gaa} + M_{Gab} = \frac{1}{G}\frac{T_{0b}}{2\pi}\left(\frac{v_{sa} + v_{sb}}{sin\theta_I}\right)^3 \qquad (A4)$$

where v_{sa} and v_{sb} represent the velocity components in the direction of the line of the sight for the Gaa and Gab BHs, respectively. In Oya's paper [23] $M_{Gaa} + M_{Gab}$ is concluded to have a median value of $4.21 \times 10^6 M_\odot$ by assuming $\theta_I \cong 90°$; but when we use $4.28 \times 10^6 M_\odot$, as concluded by Gillessen et al for $M_{Gaa} + M_{Gab}$, the expression of , θ_I is improved as,

$$\frac{4.28 \times 10^6 M_\odot}{4.21 \times 10^6 M_\odot} = \left(\frac{1}{sin\theta_I}\right)^3 . \qquad (A5)$$

From eq,(A5), θ_I can be calculated to be $83.988° \cong 84°$.

Appendix B

The ray path under the condition of intense gravity can be found by calculating the
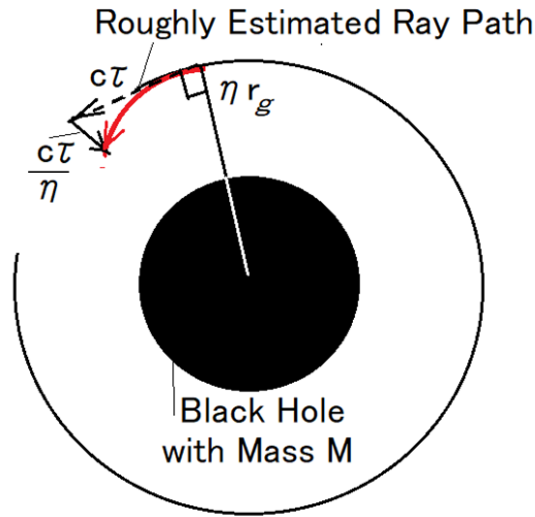
Figure B: Simple depiction of the curved ray path under the intense gravity at a point $r = \eta r_g$ with a gravity radius r_g, and a factor η where the Minkowsky system is falling with a velocity of $cV = (1/\eta)c$ towards the gravity center. Using the simplified concept of the GR, an approximated ray path is depicted for propagation in the horizontal direction; the ray shifts the position by $(1/\eta)c\tau$ toward the center of the gravity from the virtual position assumed at a distance of $c\tau$ in the horizontal direction from the starting point.

zero geodesic in the established theory of general relativity. For the purpose of the rough estimation of the ray path under the condition of intense gravity, however, we can apply a simplified approach by following the principle of the theory of general relativity. That is, when we find a Minkowsky coordinate following the free falling system, the ray path can be expressed by a straight line in that coordinate system. This means that we can draw the curved ray paths with falling processes in the vertical direction towards the center of the gravity of the massive black hole. To estimate the velocity component c_v in the vertical direction for propagating light (radiowaves) at position r, we follow the case of the Schwartzschild space time, which gives the light velocity for the vertical path $r(t)$ (for the radial distance with respective to the time t) as

$$\frac{dr}{dt} \equiv v_L = \left(1 - \frac{r_g}{r}\right)c \qquad (B1)$$

When the observation is made at a position fixed to the black hole system, the expression of eq.(B1) indicates that the resultant light velocity is expressed subtracting the free falling velocity c_v of the system under the influence of the intense gravity from the intrinsic velocity c of the light that propagates towards the outside in the free falling Minkowsky system. That is, we have the light velocity v_L in the system fixed to the black hole , as

$$v_L = c - c_V \quad \text{with} \quad c_V = \frac{r_g}{r}c \qquad (B2)$$

At the point $r = \eta r_g$, then, we can express as $c_v = (1/\eta)c$. With this simplified concept, we can depict an approximated ray path, as given in Figure B, where a ray starts to propagate in the horizontal direction at a point with a distance of ηr_g from the center of the Schwartzschild black hole. The ray shifts the position by $(1/\eta)c\tau$ towards the center of the black hole approximately from the virtual position, moving a distance of $c\tau$ in a time interval τ, in the horizontal direction from the starting point.

Appendix C

When we look up the table of observation data $f(t_m)$ in a time series with a series order m (integer), the data in the table are expressed by

$$f(t_m) = f(t) \cdot h(t, t_m) . \qquad (C1)$$

with a sampling function $h(t, t_m)$, that can be expressed by

$$h(t, t_m) = \sum_{m=1}^{M} \delta(t - t_m). \qquad (C2)$$

By applying the inverse Fourier transformation for $h(t, t_m)$, we have expression as

$$h(t, t_m) = \frac{1}{2\pi} \sum_{m=1}^{M} \int_{-\infty}^{\infty} \{cos[\omega(t - t_m)] + i \cdot sin[\omega(t - t_m)]\} \, d\omega. \qquad (C3)$$

This expression can be approximated with the discrete form to be suitable for the present discussion for sampling data at $t = t_m$ as

$$h(t, t_m) = \frac{1}{2\pi} \sum_{m=1}^{M} \sum_{k=1}^{K} cos\left[k\left(\frac{2\pi}{T_s}\right)(t - mT_s)\right]. \qquad (C4)$$

where T_s is a constant period of the data sampling time window (DSTW) .
Here, we consider the case of approximation for simple understanding of the shadow phenomena by taking the fundamental frequency for f(t) as f(t) = $A \, cos(2\pi t_m/T_{ob})$. Because we are concerned with the fundamental period of the phenomena, we can use only k=1 in eq.(C4) to express h(t). Then, it follows from eq.(C1) that

$$f(t_m) = \frac{A}{2} \, cos\left(\frac{2\pi t_m}{T_{ob}}\right) \cdot cos \ \left(\frac{2\pi}{T_s}\right)(t_m - mT_s)\right] \; \text{; for } 1 < m < M \quad (C5)$$

Then, the time variation that is the target of the fitting model is expressed by

$$f(t_m) = \frac{A}{2} \left\{\frac{1}{2} cos\left[2\pi\left(\frac{1}{T_s} + \frac{1}{T_{ob}}\right)t_m\right] + \frac{1}{2} cos\left[2\pi\left(\frac{1}{T_s} - \frac{1}{T_{ob}}\right)t_m\right]\right\}; \text{ for } 1 < m < M \ (C6)$$

When we try to fit between $f(t_m)$ and the time-varying model with the sweeping period T_{mod}, two cases of fitting results for T_{mod} can be obtained:

$$\left.\begin{array}{c} \dfrac{1}{T_{mod}} = \dfrac{1}{T_s} + \dfrac{1}{T_{ob}}, \\[4mm] \text{and} \qquad \dfrac{1}{T_{mod}} = \pm\left(\dfrac{1}{T_s} - \dfrac{1}{T_{ob}}\right). \end{array}\right\} \qquad (C7)$$

In the main text, the bottom cases in the above equation were described; the top case was not concerned, because T_{mod} is outside the discussed range. The DSTW, in the present case, consists of two categories; those are constant time interval around 1200 s   and random time interval as indicated in the main text. For the case of the random interval, the DSTW does not appear explicitly for the selection of the period in the data fitting in the time-space (direct fitting); we can understand that as is equivalent to the case of $T_s \to \infty$, in eq.(C7).

Appendix D
When we observe a time series of data $f(t_m)$ with the given observation timing t_m, it can be determined by the function $h(t, t_m)$ as

$$f(t_m) = f(t) \cdot h(t, t_m). \qquad (D1)$$

where $h(t, t_m)$ is given by

$$h(t. t_m) = \begin{cases} \displaystyle\sum_{m=M_{\eta-1}+1}^{M_\eta} \delta[t - \eta \ T_d - t_m] & \text{for } \eta T_d < t < \eta T_d + \tau_{ob}. \\[4mm] 0 & \text{for } \eta T_d + \tau_{ob} < t < (\eta+1)T_d \end{cases} \qquad (D2)$$

It should be noted that t_m is defined from the starting time of the observation period for each observation of η day; and η is defined as 0 for the first day of observation. M_η is the maximum number of observation trials where $M_{-1} = 0$. It is assumed that the observation period τ_{ob} of each observation day is the same.

The spectra of the observed data series eq.(D1) are expressed by the Fourier transformation, as

$$D(\omega) = \int_{-\infty}^{\infty} \left[\frac{1}{2\pi} \cdot \int_{-\infty}^{\infty} F(\omega_b)\, e^{i\omega_b t} d\omega_b \right] h(t, t_m) e^{-i\omega t} dt \qquad (D3)$$

where $F(\omega_b)$ is given for f(t) as

$$F(\omega_b) = \int_{-\infty}^{\infty} f(t) e^{-i\omega_b t} dt. \qquad (D4)$$

We rewrite eq.(D3) as

$$D(\omega) = \frac{1}{2\pi} \int_{-\infty}^{\infty} F(\omega_b) \left[\cdot \int_{-\infty}^{\infty} h(t, t_m) e^{-i(\omega - \omega_b)t} dt \right] d\omega_b \qquad (D5)$$

When we express the Fourier transformation for $h(t, t_m)$ for the whole observation interval of DSTW, it follows that

$$H_D(\xi) = \frac{1}{2T_d + \tau_{ob}} \int_0^{2T_d + \tau_{ob}} h(t, t_m) e^{-i\xi t} dt$$

$$= \frac{1}{2T_d + \tau_{ob}} \sum_{\eta=0}^{2} \int_{\eta T_d}^{\eta T_d + \tau_{ob}} \sum_{m=M_{\eta-1}+1}^{M_\eta} A_\eta \delta[t - \eta T_d - t_m^*] e^{-i\xi t} dt. \qquad (D6)$$

where t_m^* is newly defined in relation to the DSTW t_m as

$$t_m = \eta T_d + t_m^*, \qquad (D7)$$

for $t_m \geq \eta T_d$; M_η is the maximum number given 8 for $\eta = 0$, and 14, and 20, respectively, for $\eta = 1$, and 2. Using eq.(D6), eq.(D5) can be rewritten as

$$D(\omega) = \frac{1}{2\pi(2T_d + \tau_{ob})} \int_{-\infty}^{\infty} F(\omega_b) \left\{ \sum_{\eta=0}^{2} \left[\sum_{m=M_\eta+1}^{M_{\eta+1}} A_\eta e^{-i(\omega - \omega_b)t_m^*} \right] e^{-i(\omega - \omega_b)\eta T_d} \right\} d\omega_b .$$

$$\qquad (D8)$$

From a theoretical standpoint, we are concerned with three kinds of $F(\omega_b)$ function that are an unknown function for VLBI-Data, a combination of the sinusoidal function for the DRWP-Model, and an average of 160 cases of random noise series. To understand the coupling feature between the time variation of the phenomena and the DSTW, here, we consider the representative of $f(t) = \cos(\omega_0 t)$ to represent the time variation of the DRWP-Model taking ω_0 as parameter. The Fourier transformation $F(\omega_b)$ for f(t) is given by

$$F(\omega_b) = \int_{-\infty}^{\infty} f(t) e^{-i\omega_b t} dt = \frac{1}{2} \int_{-\infty}^{\infty} \left(e^{i\omega_0 t} + e^{-i\omega_0 t} \right) e^{-i\omega_b t} dt \qquad (D9)$$

Considering the relation with the delta function as

$$\delta(\omega_b - \omega_0) = \frac{1}{2\pi} \int_{-\infty}^{\infty} e^{i(\omega_b - \omega_0)t} dt, \qquad (D10)$$

$F(\omega_b)$ given by eq.(D9) is rewritten as

$$F(\omega_b) = \pi[\delta(\omega_b - \omega_0) + \delta(\omega_b + \omega_0)]. \qquad (D11)$$

By inserting eq.(D11) into eq.(D8), we have the spectra of the total feature $D_{DMod}(\omega)$, which is coupled with the given SDWT as

$$D_{DMod}(\omega) = \frac{1}{4(2T_d + \tau_{ob})} \left\{ \sum_{\eta=0}^{2} \left[\sum_{m=M_\eta+1}^{M_{\eta+1}} A_\eta e^{-i(\omega-\omega_0)t_m^*} \right] e^{-i(\omega-\omega_0)\eta\, T_d} \right.$$

$$\left. + \sum_{\eta=0}^{2} \left[\sum_{m=M_\eta+1}^{M_{\eta+1}} A_\eta e^{-i(\omega+\omega_0)t_m^*} \right] e^{-i(\omega+\omega_0)\eta\, T_d} \right\}. \qquad (D12)$$

It should be noted that the time series t_m^* consists of random intervals, in general, between each time interval $t_{m+1}^* - t_m^*$. When we consider a time series with a constant interval T_I, the introduction of a new function $S(\omega - \omega_0)$ is required; that is,

$$\frac{Z(\omega - \omega_0)}{\sum_{m=1}^{M_3} e^{[-i(\omega-\omega_0)mT_I]}} = S(\omega - \omega_0), \qquad (D13)$$

where

$$Z(\omega - \omega_b) = \sum_{m=1}^{M_3} e^{-i(\omega-\omega_0)t_m}. \qquad (D14)$$

Then, using the defined function, $S(\omega - \omega_0)$, eq.(D12) can be rewritten as

$$D_{DMod}(\omega) = \frac{1}{4(2T_d + \tau_{ob})} \left\{ \sum_{\eta=0}^{2} \left[\sum_{m=\eta M_s+1}^{(\eta+1)M_s} e^{-i(\omega-\omega_0)mT_I} \right] S(\omega - \omega_0)e^{-i(\omega-\omega_0)\eta T_d} \right.$$

$$\left. + \sum_{\eta=0}^{2} \left[\sum_{m=\eta M_s+1}^{(\eta+1)M_s} e^{-i(\omega+\omega_0)mT_I} \right] S(\omega + \omega_0)e^{-i(\omega+\omega_0)\eta T_d} \right\}. \qquad (D15)$$

where M_s is a constant number defined as $M_s T_I = \tau_{ob}$
Then, eq.(D15) can be further rewritten as

$$D_{DMod}(\omega) = \frac{1}{4(2T_d + \tau_{ob})} \left\{ \left[\sum_{m=1}^{M_s} e^{[-i(\omega-\omega_0)mT_I]} S(\omega - \omega_0) \right] \cdot \sum_{\eta=0}^{2} e^{-i(\omega-\omega_0)\eta T_d} \right.$$

$$\left. + \left[\sum_{m=1}^{M_s} e^{-i(\omega+\omega_0)mT_I} S(\omega + \omega_0) \right] \sum_{\eta=0}^{2} e^{-i(\omega+\omega_0)\eta\, T_d} \right\}. \qquad (D16)$$

The summation part with the data sampling timing of the constant interval T_I in the above eq.(D16) is given through normalization as

$$\frac{1}{M_s} \sum_{m=1}^{M_s} e^{-i(\omega-\omega_0)mT_I} = \frac{1}{M_s} \cdot \frac{1 - e^{-i(\omega-\omega_0)(M_s+1)T_I}}{1 - e^{-i(\omega-\omega_0)T_I}}. \qquad (D17)$$

After several steps of mathematical manipulation, it follows that

$$\frac{1}{M_s} \sum_{m=1}^{M_s} e^{-i(\omega-\omega_0)mT_I} = \frac{sin\{[(M_s + 1)/2](\omega - \omega_0)T_I\}}{M_s \cdot sin[(\omega - \omega_0)(T_I/2)]} \cdot e^{-i(\omega-\omega_0)(M_s/2)T_I}. \qquad (D18)$$

When the angular frequency ω approaches ω_0, we have an approximated expression for eq.(D18) as

$$\frac{\sin\{[(M_3+1)/2](\omega-\omega_0)T_I\}}{M_3 \cdot \sin[(\omega-\omega_0)(T_I/2)]} \cdot e^{-i(\omega-\omega_b)(M_3/2)T_{ob}} = \frac{\sin\{[(M_3+1)/2](\omega-\omega_b)T_I\}}{M_3 \cdot (\omega-\omega_b)(T_I/2)} \cdot \qquad (D19)$$

By inserting eq.(D19) into eq.(D16), we have the result

$$D_{DMod}(\omega) =$$
$$\frac{1}{4(2T_d+\tau_{ob})} \left\{ \frac{\sin\{[(M_s+1)/2](\omega-\omega_0)T_I\}}{M_s \cdot (\omega-\omega_0)(T_I/2)} e^{-i(\omega-\omega_0)(M_3/2)T_I} \right.$$

$$\left. \times S(\omega-\omega_0)\left[1+e^{-i\omega T_d}+e^{-i\omega 2T_d}\right]\right\}. \qquad (D20)$$

The last term on the right-hand-side of eq.(D16) that is given with the normalization by M_s as

$$\frac{1}{M_s}\left[\sum_{m=1}^{M_s} e^{-i(\omega+\omega_0)mT_I} S(\omega+\omega_0)\right] \sum_{\eta=0}^{2} e^{-i(\omega+\omega_0)\eta T_d}$$

is neglected because of the magnitude of order of $1/M_s$. The last part of right-hand-side of eq.(D20) is expressed as

$$1+e^{-i\omega T_d}+e^{-i\omega 2T_d} = 1+\cos[2\omega T_d]-i\sin[2\omega T_d]+e^{-i\omega T_d}$$

$$= 2\cos[\omega T_d]e^{-i\omega T_d}+e^{-i\omega T_d}. \qquad (D21)$$

Apart from the singular point used to express the VSCAT at $\omega=\omega_0$, the spectra given by eq.(D16) can be expressed as

$$D_{DMod}(\omega) = \frac{K_{DMod}}{4(2T_d+\tau_{ob})} \left[\sum_{m=1}^{M_s} e^{-i\omega mT_I} S(\omega-\omega_0)\right]$$

$$\cdot [2\cos[\omega T_d]+1] \times e^{-i\omega T_d}. \qquad (D22)$$

where K_{DMod} is a constant that is expressed by

$$K_{DMod} = \sum_{m=1}^{M_3} 2\cos(\omega_0 t_m). \qquad (D\,23)$$

By defining D_{DMod}^R and D_{DMod}^{Im} as

$$D_{DMod}^R = \sum_{m=1}^{M_s} \cos(\omega mT_I) \qquad (D24)$$

and

$$D_{DMod}^{Im} = -\sum_{m=1}^{M_s} \sin(\omega mT_I) \qquad (D25)$$

we have the expression for the absolute value of the spectra of VSCAT of the DRWP-Model as

$$|D_{DMod}(\omega)| = \frac{K_{DMod}S(\omega-\omega_0)}{4\pi(2T_d+\tau_{ob})} \sqrt{(D_{DMod}^R)^2+(D_{DMod}^{Im})^2} \{2\cos[\omega T_d]+1\}. \qquad (D26)$$

This result shows the existence of the ripple-like modulation in the full range of the spectra due to effects with the form $cos[\omega T_d]$, where the spectra show local peaks at every frequency corresponding to $\omega = 2\pi/T_d$. This is pointed out in the main text in relation to the result given in Figure 16.

For the case of the average random noise (RAND) spectra, we start with the step corresponding to eq.(D8) that is expressed by setting $F(\omega_b)$ to be a constant A as

$$D_{RAND}(\omega) = \frac{A}{2\pi(2T_d + \tau_{ob})} \left\{ \sum_{\eta=0}^{2} \left[\sum_{m=M_\eta+1}^{M_{\eta+1}} A_\eta e^{-i\omega t_m^*} e^{-i\omega\eta T_d \cdot} \times \int_{-\infty}^{\infty} \cdot e^{i\omega_b t_m^*} e^{i\omega_b \eta T_d} \, d\omega_b \right] \right\}$$

(D27)

Because $T_d \gg t_m^*$, the integration of $e^{i\omega_b t_m}$ by ω^b for large m values, which is related to $t_m > \tau_{0b}$, becomes negligible. Then, eq.(D19) can be approximately rewritten by

$$D_{RAND}(\omega) = \frac{A}{2\pi(2T_d + \tau_{ob})} \left\{ \sum_{\eta=0}^{2} \sum_{m=M_\eta+1}^{M_{\eta+1}} A_\eta e^{-i\omega t_m^*} e^{i\omega\eta T_d} \right\} \times \frac{\int_{\omega_1}^{\omega_2} e^{i\omega_b t_m^*} \, d\omega_b \cdot}{\omega_2 - \omega_1}$$

(D28)

This relation gives the result, finally, that

$$D_{RAND}(\omega) = \frac{K_{RAND}}{2\pi(2T_d + \tau_{ob})} \sum_{\eta=0}^{2} \sum_{m=M_\eta+1}^{M_{\eta+1}} A_\eta e^{-i\omega t_m^*} e^{i\omega\eta T_d}$$

(D29)

where K_{RAND} is a constant that is given, setting $A_0 = 1$, as

$$K_{RAND} = A \sum_{m=0}^{M_1} \frac{1}{it_m^*(\omega_2 - \omega_1)} \cdot \left(e^{i\omega_2 t_m^*} - e^{i\omega_1 t_m^*} \right).$$

(D30)

Except for the resultant constant K_{RAND} the result given by eq.(D27) is almost equal to the spectra of the DRWP-Model for the frequency range, apart from the singular points, which shows the existence of the VSCAT at $\omega = \omega_0$. Then, the absolute value of the RAND spectra can be expressed by

$$|D_{RAND}(\omega)| = \frac{|K_{RAND}|S(\omega - \omega_0)}{2(2T_d + \tau_{ob})} \sqrt{(D_{DMod}^R)^2 + (D_{DMod}^{Im})^2} \, \{2\cos[\omega T_d] + 1\}.$$

(D31)

As shown in main text, we can find unknown $S(\omega - \omega_0)$ and $\sqrt{(D^R_{DMod})2 + (D^{Im}_{DMod})^2}$ through numerical experiments using 160 random noise series.

Appendix E: To understand the feature of the modulation of the spectra, we start from the expression given in Appendix D with eq.(D20) and (D29), which are repeated here with slight rewritten parts as

$$D_{DMod}(\omega) = \frac{1}{2(2T_d + \tau_{ob})} \left\{ \frac{sin\{[(M_s + 1)/2](\omega - \omega_0)T_I\}}{M_s \cdot (\omega - \omega_0)(T_I/2)} e^{-i(\omega-\omega_0)(M_3/2)T_I} \right.$$
$$\left. \times S(\omega - \omega_0)[1 + e^{-i\omega T_d \cdot} + e^{-i\omega 2T_d \cdot}] \right\}.$$

(E1)

and

$$D_{RAND}(\omega) = \frac{K_{RAND}}{2\pi(2T_d + \tau_{ob})} \sum_{m=M_\eta+1}^{M_{\eta+1}} A_\eta e^{-i\omega t_m^*} \left[1 + e^{-i\omega T_d} + e^{-i\omega 2T_d}\right]. \qquad (E2)$$

In preparation for taking the absolute values of the spectra corresponding to Figure 14 in the main text, here, we define two complex quantities as

$$A_R + iA_{Im} \equiv$$

$$\frac{1}{2(2T_d + \tau_{ob})} \left\{ \frac{sin\{[(M_s + 1)/2](\omega - \omega_0)T_I\}}{M_s \cdot (\omega - \omega_0)(T_I/2)} e^{-i(\omega - \omega_0)(M_3/2)T_I} \times S(\omega - \omega_0) \right\}, \qquad (E3)$$

and

$$B_R + iB_{Im} \equiv \frac{K_{RAND}}{2\pi(2T_d + \tau_{ob})} \sum_{m=M_\eta+1}^{M_{\eta+1}} A_\eta e^{-i\omega t_m^*} \qquad (E4)$$

Then we can express

$$D_{DMod}(\omega) = (A_R + iA_{Im}) \cdot \left[1 + e^{-i\omega T_d} + e^{-i\omega 2T_d}\right]. \qquad (E5)$$

Further, eq.(E5) can be rewritten as

$$D_{DMod}(\omega) = A_R\{1 + cos[\omega T_d] + cos[\omega 2T_d] + A_{Im}\{sin[\omega T_d] + sin[\omega 2T_d]\}\}$$

$$+ i\{A_{Im}\{1 + cos[\omega T_d] + cos[\omega 2T_d]\}$$

$$- A_R\{sin[\omega T_d] + sin[\omega 2T_d]\}\}. \qquad (E6)$$

The absolute value of $D_{DMod}(\omega)$ is then expressed by

$$D_{DMod}(\omega) = (A_R^2 + A_{Im}^2)^{1/2}\{3 + 4cos[\omega T_d] + 2cos[\omega 2T_d]\}^{1/2}. \qquad (E7)$$

After a few steps of the mathematical manipulation eq.(E7) can be rewritten by

$$D_{DMod}(\omega) = (A_R^2 + A_{Im}^2)^{1/2}\{1 + 2cos[\omega T_d]\}. \qquad (E8)$$

For the case of $D_{DMod}(\omega)$ we arrive at similar results by replacing A_R and A_{Im} with B_R and B_{Im}, respectively, which gives

$$D_{DMod}(\omega) = (B_R^2 + B_{Im}^2)^{1/2}\{1 + 2cos[\omega T_d]\}. \qquad (E9)$$

Thus, we can see that eqs. (E8) and (E9) show periodic modulation with a frequency interval of $\Delta f = 1/T_d$.